

A Rocket Spectroscopic Payload in Support of the Apollo Telescope Mount Experiments

(NASA-CR-141117) A ROCKET SPECTROSCOPIC PAYLOAD IN SUPPORT OF THE APOLLO TELESCOPE MOUNT EXPERIMENTS Final Report (Aerospace Corp., El Segundo, Calif.) 80 p HC \$4.75	N75-13003 Unclas CSCL 22C G3/12 17141
--	---

Prepared by SPACE ASTRONOMY PROJECT
Space Physics Laboratory

5 July 1974



Prepared for
NATIONAL AERONAUTICS AND SPACE ADMINISTRATION
Washington, D. C.

Contract No. NASW-2361



Laboratory Operations

THE AEROSPACE CORPORATION

A ROCKET SPECTROSCOPIC PAYLOAD IN
SUPPORT OF THE APOLLO TELESCOPE
MOUNT EXPERIMENTS

Prepared by
Space Astronomy Project
Space Physics Laboratory

5 July 1974

Laboratory Operations
THE AEROSPACE CORPORATION
El Segundo, California

Prepared for
National Aeronautics and Space Administration
Washington, D.C.


Contract No. NASW-2361

PREFACE


The major contributors to this rocket experiment were R. L. Williams, W. H. Brown, J. F. Durana, A. G. Harper, T. H. Higa, E. M. Irwin, D. A. Jones, D. L. McKenzie, D. A. Roux, H. R. Rugge, J. H. Underwood, A. B. C. Walker, Jr., and R. M. Young.

A ROCKET SPECTROSCOPIC PAYLOAD IN
SUPPORT OF THE APOLLO TELESCOPE
MOUNT EXPERIMENTS

Prepared


H. R. Rugge, for
Space Astronomy Project

Approved


G. A. Paulikas, Director
Space Physics Laboratory

ABSTRACT

The scientific instrumentation and other payload systems of a NASA-sponsored solar rocket experiment are described in detail. The payload was designed and built by the Space Astronomy Project of The Aerospace Corporation to carry out high-resolution spectroscopic measurements of the solar corona. The objectives of the rocket payload were: (1) to carry out high-spectral-resolution measurements of a coronal active region in the x-ray and extreme ultraviolet regions at the same time as high-spatial-resolution measurements were being made of the same active region by the Apollo Telescope Mount experiments flown on Skylab; and (2) to derive a physical model of the conditions in the coronal active regions, which dominate the x-ray spectrum of the nonflaring active sun, on the basis of data obtained from both the rocket instrumentation and several of the Apollo Telescope Mount experiments.

PRECEDING PAGE BLANK NOT FILMED

CONTENTS

PREFACE	ii
ABSTRACT	iii
I. INTRODUCTION	1
II. ROCKET INSTRUMENTATION MECHANICAL CONFIGURATION	5
A. Basic Support Structure	5
B. Instrument Location	5
III. BRAGG CRYSTAL SPECTROMETERS	11
A. X-ray Analyzing Crystal Properties	11
B. Crystal/Detector Drive Mechanism	12
IV. GRATING SPECTROMETER SYSTEM DESCRIPTION	15
A. Grazing Incidence Gratings	15
B. Grating Drive	18
V. COLLIMATORS	19
A. Introduction	19
B. Mechanical Design of Entrance Collimators	22
C. Experimental Measurements	24
D. Collimator Alignment With the Solar Aspect System (SPARCS)	33
E. Grating Exit Collimator Description	34
F. Entrance Collimator Mounting	35
G. Grating Exit Collimator Mounting	35
VI. DETECTOR SYSTEMS	37
A. Introduction	37
B. Flow Proportional Counter Construction	38
C. Detector Window Properties	38

CONTENTS (Continued)

D.	Rise-Time Discrimination	41
E.	Detection Electronics	44
F.	Flow Gas Control System	52
VII.	GRAZING INCIDENCE X-RAY TELESCOPE	65
VIII.	MONITOR PROPORTIONAL COUNTER SYSTEM	67
A.	Description	67
B.	Monitor System Calibration	70

TABLES

1.	Major Rocket Instrument Parameters	3
2.	Results of X-ray Entrance Collimator Alignment Tests	28
3.	Measured Effective Values of Collimator Transmission Factor	32
4.	Rocket Detector System Parameters	37
5.	Detector Window Effective Thicknesses	39
6.	Rise Time Discrimination vs Pressure Data Obtained at 2 Å	45
7.	Rise-Time Discrimination vs Wavelength Data Obtained at a Pressure of 180 mm of Hg	46

FIGURES

1.	Side View of the Main "I" Beam Structure with Electronic Cards Mounted in Place	6
2.	View of X-ray Crystal Spectrometer Instrumentation Mounted in Flight Configuration	7
3.	View of the Grating Spectrometers and X-ray Telescope Mounted in Flight Configuration	8
4.	Entrance Apertures of all Spectrometers and X-ray Telescope as Viewed from the Solar Direction	9
5.	Diagram of a Simple McGrath-Type Collimator	20
6.	View of an X-ray Entrance Collimator with its Cover Removed	23
7.	Experimental Arrangement for the X-ray Collimator Principal Axis Determination	27
8.	Experimental Arrangement for the X-ray Transmission Measurements	30
9.	X-ray Spectrometer Detector Window/Grid Transmission Measurements vs Wavelength	40
10.	X-ray Spectrometer Detector Gas Absorption Efficiency vs Wavelength	42
11.	Grating Spectrometer Detector Gain vs Applied High Voltage for a Number of Internal Gas Pressures	43
12.	Efficiency of Detection of X rays (Fe^{55} source) and Charged Particles (Co^{60} source) vs Rise-Time Discrimination Circuit Time Constant for an Argon, Xenon, Methane Filled Detector	47
13.	Efficiency of Detection of X rays (Fe^{55} source) and Charged Particles (Co^{60} source) vs Rise-Time Discrimination Circuit Time Constant for the Grating Spectrometer and an Argon, Methane (P-10 gas) Filled Detector	48

FIGURES (Continued)

14.	Block Diagram of Flow Proportional Counter Electronics	49
15.	Block Diagram of the Grating Spectrometer Gas Control System	54
16.	View of Aft Section of Rocket Payload Showing Mechanical Components of Gas Handling System for the Flow Proportional Counters	55
17.	Block Diagram of the Grating Spectrometer Electronic Pressure Control and Peripheral Electronics	57
18.	Block Diagram of the Crystal Spectrometer Gas Control System	61
19.	Block Diagram of the Crystal Spectrometer Electronic Pressure Control	63
20.	Block Diagram of the Monitor Proportional Counter System	68

I. INTRODUCTION

This report describes in some detail the scientific instrumentation and other payload systems of a NASA-sponsored solar rocket. The payload was designed and built by the Space Astronomy Project of The Aerospace Corporation to carry out high-resolution spectroscopic measurements of the solar corona. There were two major objectives for this rocket payload: (1) to carry out high-spectral-resolution measurements of a coronal active region in the x-ray and extreme ultraviolet (XUV) wavelength regions at the same time as high-spatial-resolution measurements were being made of the same active region by the Apollo Telescope Mount (ATM) experiments flown on Skylab; and (2) to derive a physical model of the conditions in the coronal active regions, which dominate the x-ray spectrum of the nonflaring active sun, on the basis of data obtained from both the rocket instrumentation and several of the ATM experiments.

The x-ray and XUV experiments on the ATM making measurements below 300 Å wavelength have excellent spatial resolution, but lack sufficiently high spectral resolution to permit construction of a detailed physical model of enhanced coronal regions in spite of the inclusion of an objective grating on the x-ray telescope provided by the American Science and Engineering (AS&E) group. The combination of high-spectral-resolution data from the rocket payload and the ATM high-spatial-resolution x-ray images can create a powerful observational base for an improved understanding of the temperature and density structure and composition of coronal condensations and flaring material. This would, in turn, provide an improved understanding of the relative importance of radiative and conductive cooling for coronal condensations and flaring material and of their total energy dissipation and budget. The observations will also complement the Harvard UV spectroheliograph on ATM by extending the range of observed spectral lines to the highest coronal temperature ranges. The complete coronal model, which can be provided by the solar rocket instrumentation described herein in conjunction with the ATM x-ray imaging telescopes (S-054 from AS&E and S-056

from Marshall Space Flight Center/Aerospace), combined with the transition region model, which can be obtained from the Harvard EUV spectrograph (S-055) experiment, should lead to a significant improvement of our understanding of the energy budget of the solar atmosphere.

In order to meet the objectives stated above, a complex highly sophisticated rocket payload was designed. It was desirable to consider as wide a range of wavelengths as feasible in order to provide as much data as possible about the solar atmosphere in an active region. Therefore, it was decided to fly grazing incidence gratings as well as Bragg crystal spectrometers to provide the principal high-spectral-resolution data. This approach made it possible to gather spectral data between 3 and 300 Å. In order to isolate a single active region for study and prevent "background" from other centers of activity, these instruments were collimated such that only one active region contributed to the measured intensities of x-ray and XUV radiation.

In addition to the crystal spectrometers and grazing incidence gratings, a glancing incidence x-ray telescope/filterwheel-camera system was flown. The filters were similar to those flown on the ATM S-056 experiment. This instrument was designed to serve two purposes: (1) to permit direct comparison of the rocket x-ray pictures with those taken on the ATM, and (2) to verify the solar pointing of the solar aspect system (SPARCS) solar pointing control, which stabilizes and properly points the rocket payload at the appropriate solar active region. The final scientific instrument was a thin-windowed proportional counter with an eight-channel pulse height analyzer for provision of crude spectral information at wavelengths shorter than 10 Å and with a temporal resolution much better than 1 sec in the event of a flare occurrence during the rocket observation. In addition, count rate changes in this detector could imply a lack of stability in the SPARCS pointing control.

A summary of the major rocket instrumentation and some of the pertinent parameters are given in Table 1. Each of these instruments as well as other major rocket subsystems are discussed in detail in subsequent sections.

Table 1. Major Rocket Instrument Parameters

Instrument	Wavelength Range, Å	Resolution	Effective Aperture Size, cm ²	Spatial Resolution on Solar Disk
RAP crystal spectrometer	7.8-25.5	$\lambda/\Delta\lambda \approx 5 \times 10^2$ at 20 Å	51.6	2.1 arc min × 1.4 arc min (along direction of dispersion)
ADP crystal spectrometer	3.2-10.4	$\lambda/\Delta\lambda = 10^3$ at 9 Å	51.6	Same as above
Short λ XUV grating spectrometer	20-220	$\lambda/\Delta\lambda = 10^2$ at 100 Å	5.2	Same as above
Long λ XUV grating spectrometer	128-400	$\lambda/\Delta\lambda \approx 2.5 \times 10^2$ at 400 Å	8.7	Same as above
X-ray telescope/ filterwheel-camera	5-60	$\Delta\lambda = 10$ Å; 8 filters of 5 materials of varying thickness	1.6	~20 arc sec
Proportional counter	2-10	8 channels; $\lambda/\Delta\lambda \approx 10$	1.27	2.1 arc min × 1.4 arc min (along direction of dispersion)

II. ROCKET INSTRUMENTATION MECHANICAL CONFIGURATION

A. BASIC SUPPORT STRUCTURE

The rocket instrumentation had to be confined to a volume defined by a cylindrical shape 15 in. in diameter and about 50 in. high. The rocket's skin could not be used as a structural member to support the instrumentation and, in fact, had to be isolated from it for two reasons: (1) aerodynamic heating of the skin to high temperatures would cause excessive payload heating and, (2) thermal expansion of the skin would stress the payload optical bench. An "I" beam supporting structure was selected as the most efficient configuration. This form of support structure offers easy mounting of various payload elements. One end of the "I" beam is welded to a bulkhead that is part of a short cylindrical section; this section accepts the cylindrical skin that surrounds the payload. The bulkhead also serves as a pressure barrier and heat sink. The uppermost section of the "I" beam extends well into the nose cone area to provide protection on landing.

The total payload weight allowance was 166.5 lb including the skin. The actual flight weight was 143 lb for the payload plus 6 lb of balancing weight. The "I" beam/bulkhead combination accounted for 47 lb of this weight.

The location of the major instruments on the "I" beam is discussed below. The sides of the "I" beam served as a convenient mounting surface for electronic circuit boards. A side view of the "I" beam with electronic cards mounted in place is shown in Fig. 1.

B. INSTRUMENT LOCATION

The locations of the major instruments (Table 1) on the "I" beam structure are shown in Figs. 2, 3, and 4. The two identical Bragg crystal spectrometer collimators, the crystals themselves, and the detectors are shown

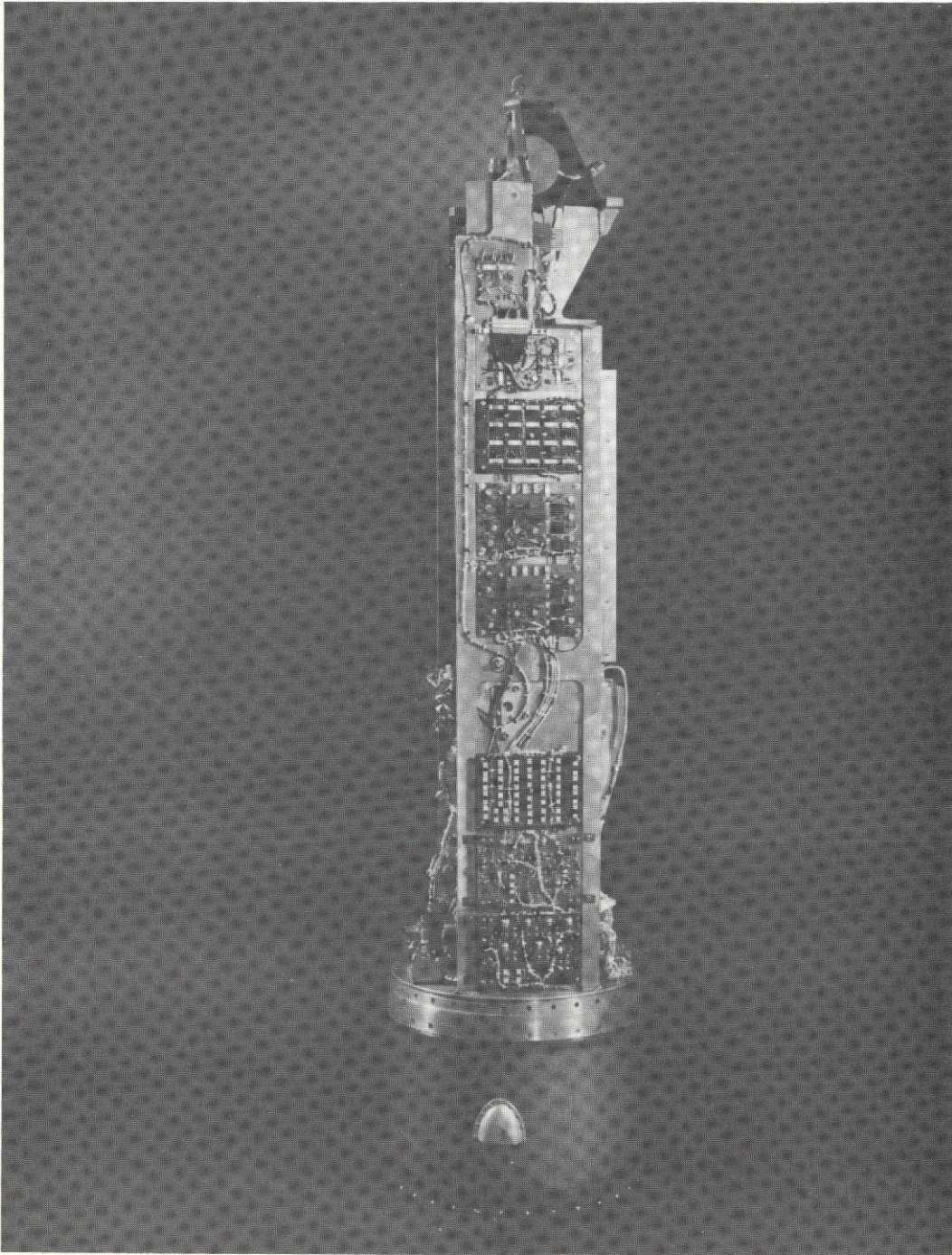


Figure 1. Side View of the Main "I" Beam Structure with Electronic Cards Mounted in Place

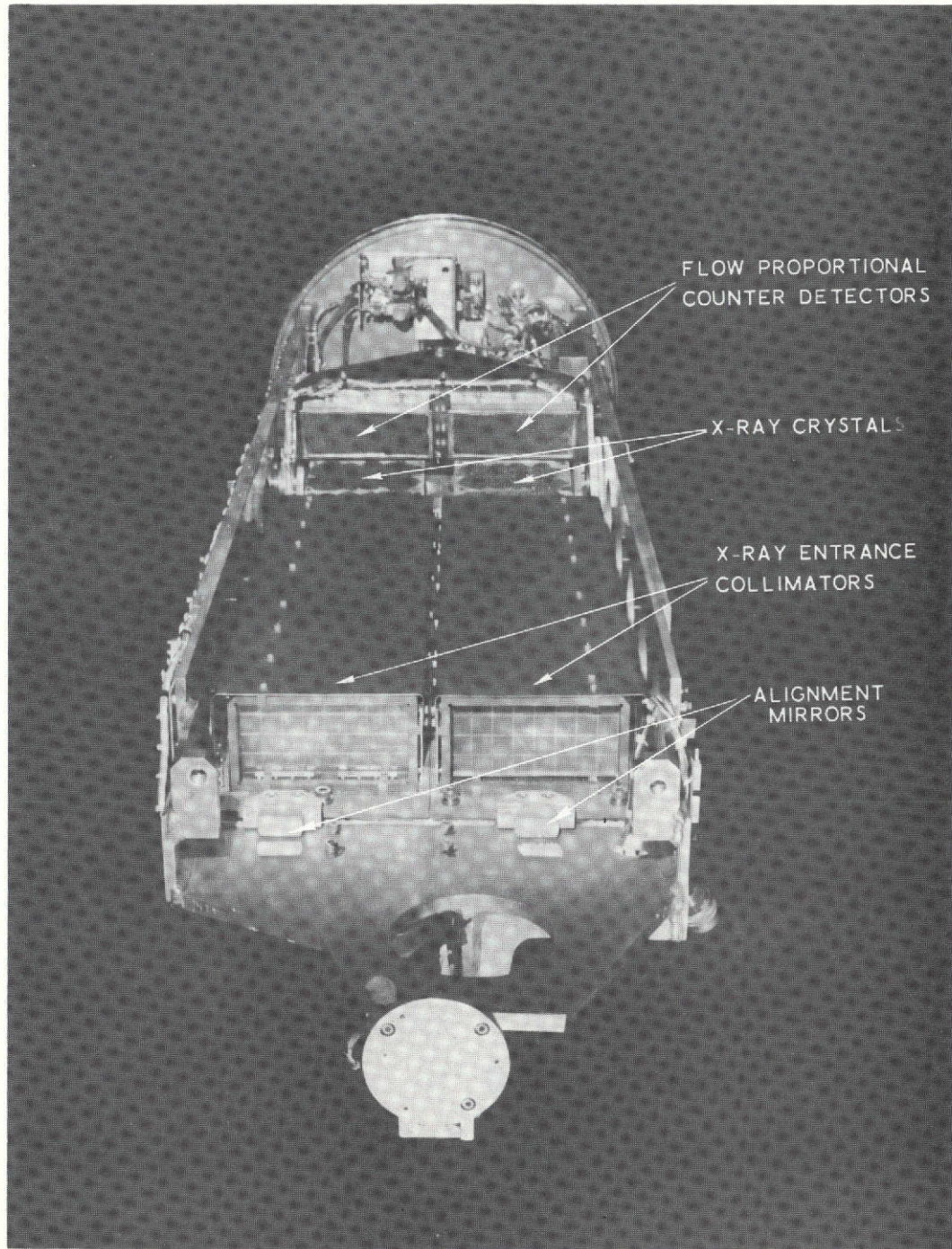


Figure 2. View of X-ray Crystal Spectrometer Instrumentation Mounted in Flight Configuration

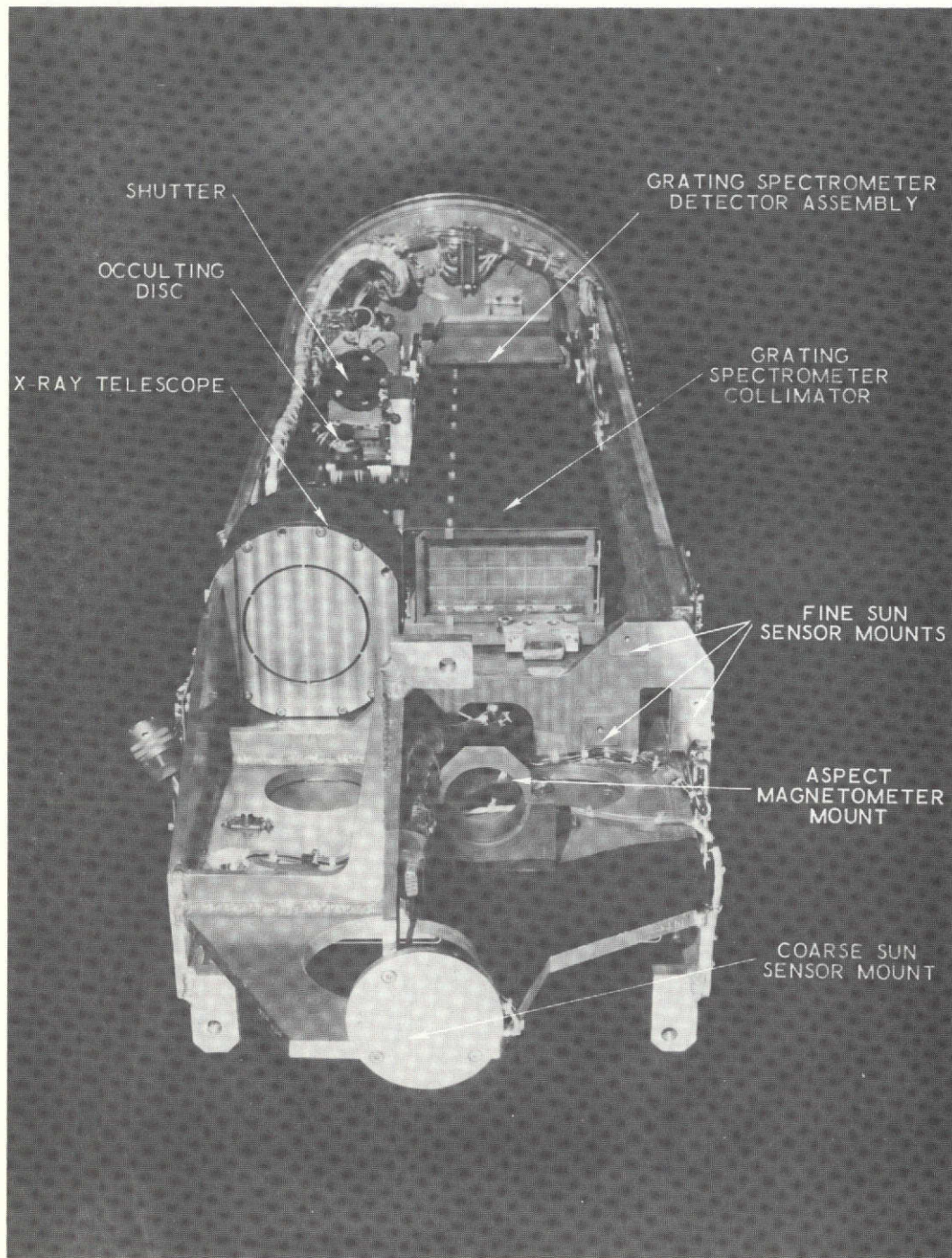


Figure 3. View of the Grating Spectrometers and X-ray Telescope Mounted in Flight Configuration

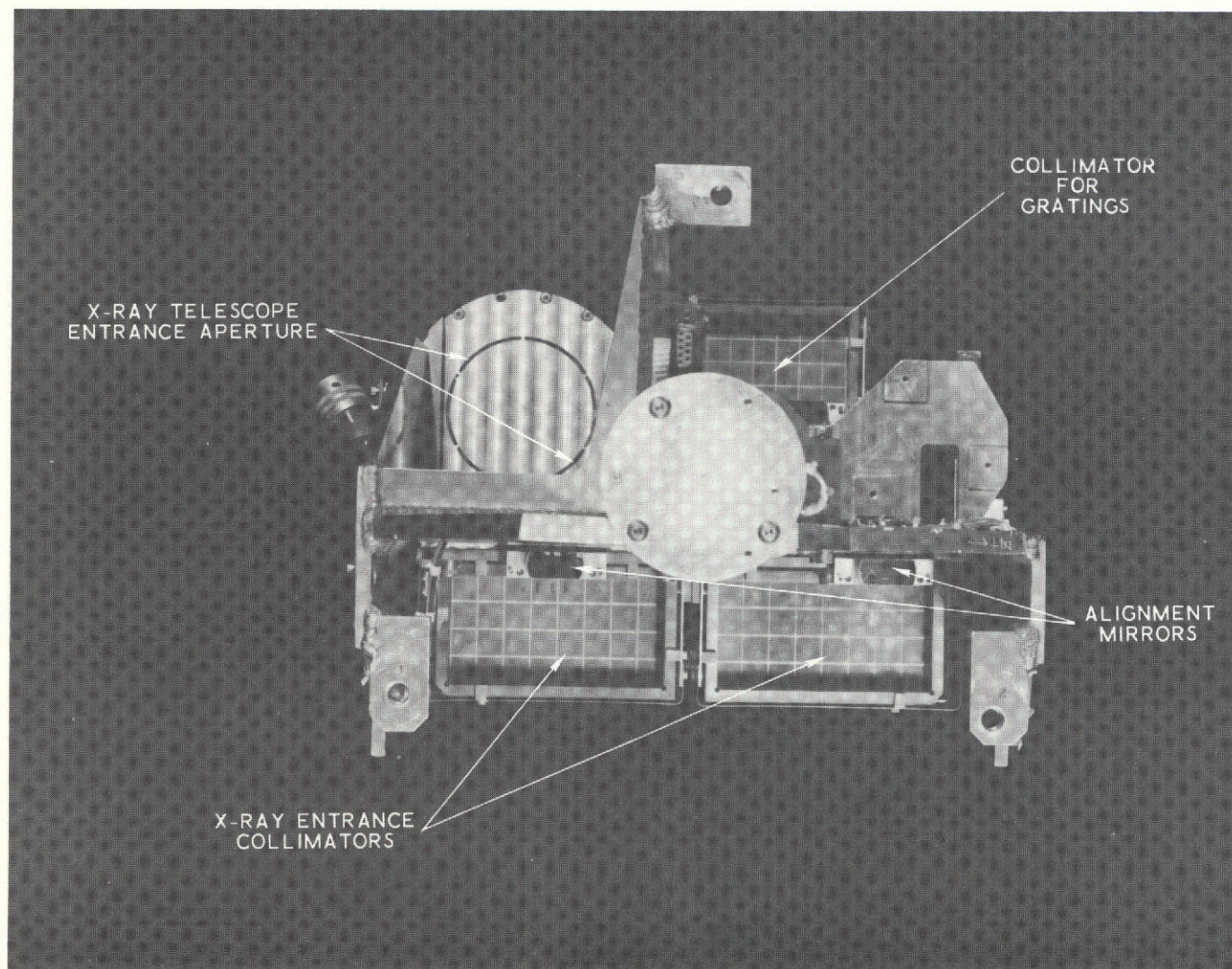


Figure 4. Entrance Apertures of all Spectrometers and X-ray Telescope as Viewed from the Solar Direction

in Fig. 2; crude detector collimation is provided by a honeycomb material. The opposite side of the "I" beam is shown in Fig. 3. It contains the single collimator that was used by both grazing incidence gratings, the x-ray telescope and shutter mechanism, the mounting plates for the aspect system, the coarse sun sensor, the fine sun sensor, and the magnetometers. A "sun's-eye" view of the payload with the three entrance collimators, the x-ray telescope aperture, and the sun sensor mounting plates is shown in Fig. 4.

III. BRAGG CRYSTAL SPECTROMETERS

A. X-ray Analyzing Crystal Properties

The two Bragg crystal spectrometers consist of a small-field-of-view collimator to define a fixed region on the solar disc, an x-ray analyzing crystal, and a thin-windowed flow-proportional counter. The crystal properties and the crystal/detector drive mechanisms are discussed in this section; the collimators and the detector systems are discussed in Sections V and VI, respectively. The crystal spectrometers are shown in Fig. 2.

The purpose of the multigrid collimators was to define a fixed field of view of 2.06×1.38 arc min (FWHM) on the solar disc. The x rays from this region are passed by the collimator and those that satisfy the Bragg conditions as the crystal/detector assembly scans are detected by the flow proportional counter.

Two different Bragg crystals were selected for this payload: rubidium acid phthate (RAP), with a 2d spacing of 26.12 \AA ; and ammonium dihydrogen phosphate (ADP), with a 2d spacing of 10.648 \AA . These crystals were mounted on a common shaft and driven by the same mechanism, described in detail in the following section. The angular range of motion of the shaft was set such that ADP covered wavelengths of 3.20 to 10.40 \AA and RAP covered wavelengths of 7.85 to 25.48 \AA . The height of the crystals (measured in the direction of the rotation axis) was equal to the collimator dimension in this direction, 10 cm. The crystals were made much wider than the collimators, however, to avoid loss of projected crystal area at low Bragg angles. The crystals were 14.2 cm wide, which meant that, at the lower end of the wavelength range covered by each spectrometer, the crystal intercepted approximately 50 percent of the beam transmitted by the collimator. The two crystals were each made from two separate 10×7.1 cm crystal sections because single crystals of the required size were not readily obtainable. Of course, the two separate sections of each crystal array had to be accurately aligned to one another in order to obtain a resolution that

compared favorably with that obtainable from a single crystal. This was done by affixing each crystal section to its own mounting plate with epoxy resin. These mounting plates were then attached to the main large crystal mount plate by three screws, each of which could be adjusted for alignment of the crystals as required.

The crystal spectrometers were programmed to provide three complete scans over this wavelength range during the useable time available above ≈ 100 km. Basic parameters for the crystal spectrometers are given in Table 1.

B. CRYSTAL/DETECTOR DRIVE MECHANISM

The crystal motion is limited to rotation from $17^{\circ}30'$ and $77^{\circ}30'$ relative to the sun line. The detector motion is geared to the crystals at a ratio of 2:1 to satisfy the Bragg condition. The motion of its normal line is limited by stops at 35 and 155° . In order to facilitate alignment, the physical capability of 0 to 90° on the crystal and 0 to 180° on the detector is possible with the stops removed.

The drive motor is a size 11 permanent magnet stepper motor with a 90° step angle. An integral gearhead with a ratio of 1718.86 is attached to the motor. The gearhead has a slip clutch on its output shaft, set to 45 oz-in., for protection of the very small gear from excessive loads that arise from manual rotation, impact with the stops, and shock or vibration. The clutch also protects against damage from full motor torque if the load is stalled.

The overall gear ratio is: motor to crystal, $8 \times 1718.86 = 13750.88$; and motor to detector, $4 \times 1718.86 = 6875.44$. Torque at the clutch divides between the crystal (at 8:1) and detector (at 4:1) as required. The crystal rotation per motor step is 23 arc sec.

The crystal traverse time (from $17^{\circ}30'$ to $77^{\circ}30''$) was specified as ≈ 100 sec; thus, the motor speed required was ≈ 91.67 steps/sec.

The ball bearings for the crystal axis are arranged such that the upper bearings are a preloaded pair with a preload of 0 to 5 lb. The lower bearing floats axially. This design effectively removes endplay, structural deflection, and thermal problems that might occur if preloading were attempted between bearings at the extreme shaft ends. An identical arrangement is used for the coaxial bearings that support the detector.

For angular position indication, a single-turn potentiometer was geared to the detector gear. Mechanical travel was 96 percent of electrical travel. Limit switches were provided at the positive stops to indicate the need to reverse.

IV. GRATING SPECTROMETER SYSTEM DESCRIPTION

A. GRAZING INCIDENCE GRATINGS

As discussed in Section I, the purpose of the grating system was to extend the wavelength coverage of the rocket instrument into the spectral region $>27 \text{ \AA}$, which was covered on Skylab by the titanium filter on the Skylab ATM S-056 experiment and the thin plastic filters on the S-054 experiment as well as the lower end of the range of the S-055 UV spectroheliograph. Therefore, the grating system was required to provide the following:

1. Wavelength coverage from ~ 20 to $\sim 400 \text{ \AA}$.
2. Spatial resolution similar to that of the crystal spectrometers.
3. Spectral resolution sufficient to resolve important spectral lines (such as Si XI (303.31 \AA) and He II (303.78 \AA); about 0.1 \AA was considered to be a good resolution to aim for.
4. Efficiency sufficient to give good statistics in the scan time available, about 100 sec per complete wavelength scan.
5. Accurate calibration at several points in the EUV spectrum to permit good measurement of the sensitivity of the ATM instruments.

There are several ways to obtain combined spatial and spectral resolution in a solar EUV spectrometer, e.g., some experimenters have used grazing incidence optics as fore-optics to feed a concave grating spectrometer. For this particular rocket experiment, an approach similar to that adopted by Bedo and Hinteregger was chosen.

In this scheme, an entrance collimator is used to define the angle of incidence on a plane grating and also to select the area of the sun to be studied. An exit collimator must be used to define the angle of diffraction, otherwise the spectra would overlap excessively, and the data would be so complicated as to be meaningless.

In order for the grating systems to have the same spatial resolution as the crystal systems, and in the interest of standardization, essentially identical entrance collimators were used for both the crystal and grating

spectrometers. These were of the multigrad (McGrath) type and are described in detail in Section V. Two spectrometers were required in order to efficiently cover the wavelength range of 20 to 400 Å. The 2-in. width of the collimators permitted two gratings to be nested such that one collimator served for both the spectrometers.

A size of 10 × 10 cm was selected for the ruled area of the gratings. It was originally intended to buy gratings that complied with specifications "off the shelf;" however, this was not possible and the gratings had to be specially ruled.

The design parameters of the two spectrometers were:

Spectrometer A (short wavelength):

Wavelength range	20-220 Å
Angle of incidence	87°
Grating ruling	1800 lines/mm
Blaze wavelength	134 Å
Blaze angle	5°
Maximum diffraction angle (20 Å)	84°18'
Minimum diffraction angle (220 Å)	73°34'
Range of diffraction angles	10°44'
Dispersion of instrument at 20 Å	0.161 Å/arc min
Dispersion of instrument at 100 Å	0.316 Å/arc min

Spectrometer B (long wavelength):

Wavelength range	128-400 Å
Angle of incidence	85°
Grating ruling	2400 lines/mm
Blaze wavelength	300 Å
Blaze angle	10°22'
Maximum diffraction angle (128 Å)	74°55'
Minimum diffraction angle (400 Å)	64°11'
Range of diffraction angles	10°44'
Dispersion of instrument (400 Å)	0.527 Å/min

The spectrometers were designed to have the same angular range of diffraction angles. Thus, the two exit collimators and the two detectors could be mounted on one arm and scanned together, which permitted a simplification of the design.

During the design of these spectrometers, it became evident that the required resolution of 0.1 \AA would be difficult to obtain without making the apertures in the exit collimators impractically small. The resolution requirement was therefore relaxed somewhat to about 1 \AA . This meant that the grating subsystem became less useful spectroscopically. It was hoped, however, that the accurate calibration to be performed on it in the EUV region would still permit its use for determination of the sensitivity of the ATM experiments.

The apertures in the exit collimators are 0.006 in. wide and 0.063 in. long. Thus, the resolutions of the two spectrometers, as a result of the angular divergence of the entrance and exit collimators, were:

Spectrometer A (short wavelength):

FWHM resolution at 20 \AA	0.360 \AA
FWHM resolution at 100 \AA	0.784 \AA

Spectrometer B (long wavelength):

FWHM resolution at 400 \AA	1.425 \AA
--------------------------------------	---------------------

In this type of plane grating spectrometer, the diffracted beam is wider than the incident beam. The beam is at its widest for the longest wavelength (400 \AA) diffracted from the long wavelength grating, 43.6 mm. This meant that very large detectors had to be used in the grating systems. Because photoelectric detectors such as channeltrons or funneltrons were not available in the size required, proportional counters were selected. As mentioned in Section VI, the same detector design was used for both grating and crystal spectrometers. It was intended to use the thinnest possible plastic windows for the grating spectrometers for maximum detector efficiency in the EUV region. This meant that the gas handling system had to supply gas at a pressure considerably less than 1 atm.

B. GRATING DRIVE

The two gratings are mounted on a structure behind an entrance collimator. The surface of one is at 3° to the sun line and the other is at 5° . The exit collimators and detectors are mounted on a common movable structure behind the gratings. The movable structure rotates a total of $10^\circ 44'$. The exit collimator behind the 3° grating rotates from $9^\circ 22'$ to $20^\circ 06'$ relative to the sun line. Similarly, the exit collimator behind the 5° grating rotates from $20^\circ 06'$ to $30^\circ 50'$. Positive stops limit the motion at the above values.

The aft end of the movable structure contains a gear sector that is driven by a unit much like that used on the crystal drive, i.e., the motor, gearhead, slip clutch, and drive gears are similar. The overall gear ratio, motor to exit collimators, is 64,170.77. The angle per motor step is 5 arc sec. The traverse time for the $10^\circ 44'$ was specified as ≈ 100 sec, which led to a motor stop rate of ≈ 76.52 steps/sec.

The pivot axis is at the center of the two gratings; thus, the exit collimators, detectors, and movable structure are cantilevered more than a safe distance. Therefore, in order to provide additional support, bearings that acted as wheels rolling on the fixed structure were used to carry most of the load.

For position indication, a single-turn potentiometer was geared to the sector gear. Mechanical travel was 94 percent of electrical travel. Limit switches were provided at the positive stops to indicate the need to reverse.

V. COLLIMATORS

A. INTRODUCTION

Satellite-borne x-ray experiments have used uncollimated Bragg crystal spectrometers to measure x-ray emission from the entire solar disk. Since the sun is a finite sized object, and the condition for Bragg reflection

$$n\lambda = 2d \sin \theta$$

combines spatial and spectral resolution, the use of an uncollimated spectrometer can result in erroneous wavelength measurements or anomalously broad emission lines. The rocket payload avoids (or minimizes) these problems by using fine collimators to select a small region on the sun for observation. Thus, the collimator makes a known contribution to the spectral line width (if we assume that the emitting region fills the aperture) and the wavelength uncertainty is approximately

$$\Delta\lambda = 2d \cos \theta \Delta\theta$$

in first order.

The crystal and grating spectrometers use multigrid mechanical entrance collimators to isolate a region 1.38×2.06 arc min FWHM on the sun. The collimators are based on a design by McGrath.

A diagram of a simple McGrath collimator is given in Fig. 5. It is constructed as follows. The outermost grids are placed first, a distance L apart. A ray is then drawn from the leftmost corner of an upper grid opening through the leftmost corner of the adjacent lower grid opening, and plate 1 is placed to just block this ray. By similar triangles

$$\frac{W}{L - \ell_1} = \frac{W + t}{L} \quad \text{or} \quad \ell_1 = \frac{t}{W + t} L$$

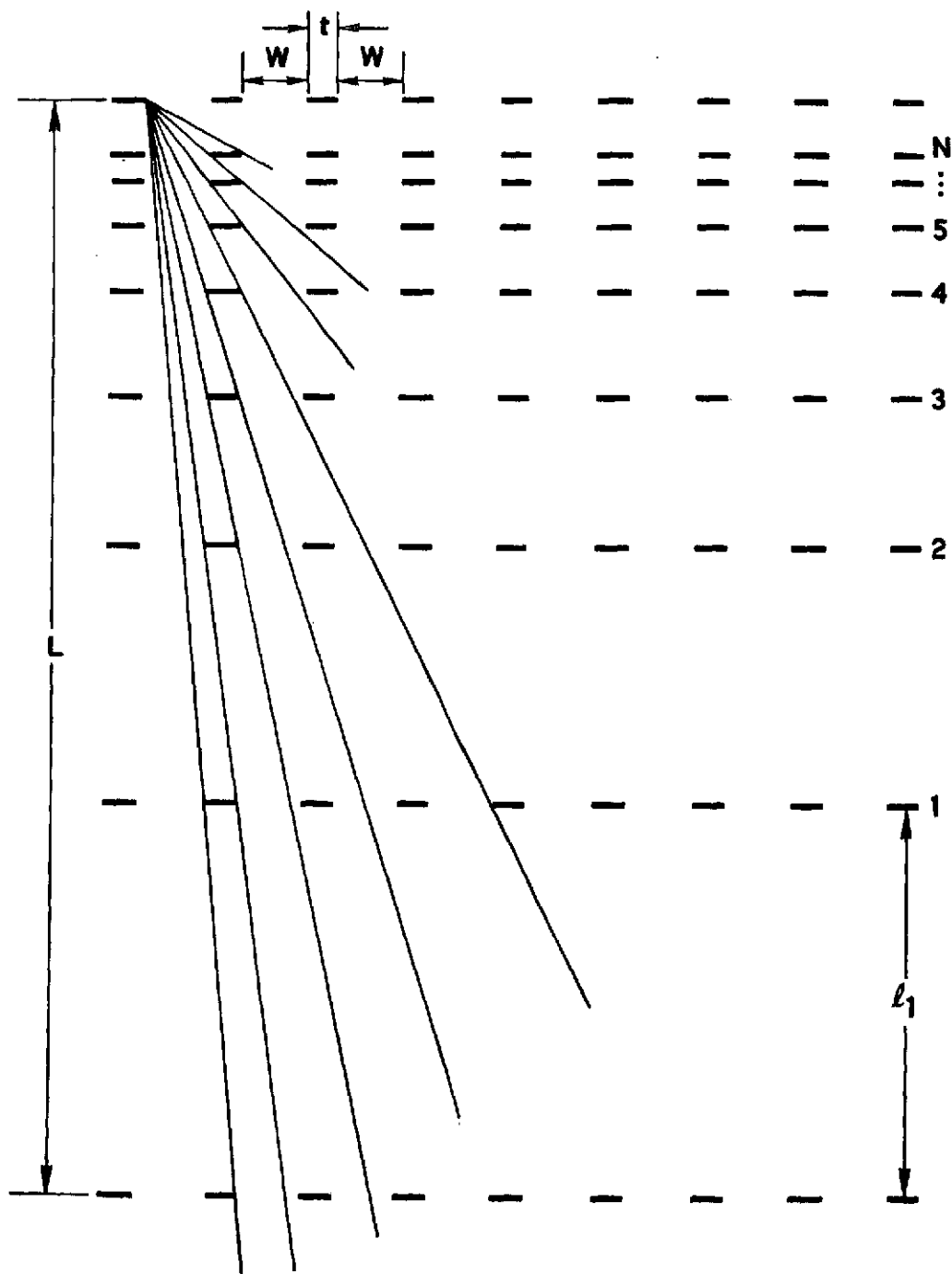


Figure 5. Diagram of a Simple McGrath-Type Collimator

For grid 2, the above procedure is repeated with grid 1 replacing the bottom grid, and so on. Thus,

$$\frac{W + t}{L - \ell_{n+1}} = \frac{W}{\ell_{n+1} - \ell_n}$$

Solving this equation leads to a general formula

$$\ell_n = L \left[1 - \left(\frac{W}{W + t} \right)^n \right]$$

Following this procedure assures that no radiation will leak through the collimator from the left edge of the openings at any angle below θ_M , where

$$\tan \theta_M = \frac{W + t}{L - \ell_n} = \frac{(W + t)^{N+1}}{LW^N}$$

and N is the total number of intermediate grids placed. Note that small side lobes may occur because of radiation striking the upper grid at points other than at the edge of the opening. The minimum angle for such a side lobe is given by

$$\tan \theta_M = \frac{t}{L - \ell_n} = \frac{t}{L} \left(\frac{W + t}{W} \right)^N = \left(\frac{t}{W + t} \right) \theta_M$$

Such side lobes are not forbidden by the design technique. Generally, they are not a problem. Note that the grid placement depends only on $W/W + t$; thus, for two-dimensional grids, this ratio should be equal in both dimensions. For such a collimator, the angular resolution is $\tan^{-1}(W_x/L) \times \tan^{-1}(W_y/L)$, and the area transmission factor is $(W/W + t)^2$.

The rocket entrance collimators had $N = 10$, $W/(W + t) = 2/3$, $L = 15$ in., $W_x = 0.006$ in., and $W_y = 0.009$ in. Following the McGrath design, we would have had an angular resolution of 82×123 arc sec, $\theta_{Mx} = 119$ arc min, $\theta_{My} = 178$ arc min, and an area transmission factor of 0.44. However, the McGrath design is difficult to construct because, for high n , the grids nestle closer and closer together and it becomes difficult to place the grids accurately and rigidly. In order to overcome this problem, some of the high- n grids were moved to other locations in the collimator. For example, the n^{th} grid ended up a distance $\ell_n - \ell_{n-1}$ behind the k^{th} grid, where $k < n - 1$. This preserves most of the intergrid spacings, but does not necessarily preserve the transmission properties of the McGrath collimator. However, the positions of the first seven grids remained unchanged, and the formulas developed here could be used to place a lower limit on expected collimator performance. Accordingly, no major side lobes were expected below $\theta_{Mx} = 35.2$ arc min and $\theta_{My} = 53$ arc min. Since the solar diameter is ≈ 32 arc min, this collimation is adequate for a solar measurement. A view of one of the x-ray entrance collimators with its cover removed is shown in Fig. 6.

The collimator was computer tested to verify the design. From 11 evenly spaced points in a single top-grid opening, rays were generated at angles to the collimator axis, increasing from 0° in 0.1 arc min steps. A small side lobe in the x direction with a maximum transmission of 20 percent was found between 33.5 and 34.1 arc min. Such a side lobe would be important only if the solar target lay above the limb. There were no other side lobes below 55 arc min.

B. MECHANICAL DESIGN OF ENTRANCE COLLIMATORS

Because it is not possible to use optical methods to look through 12 finely spaced grids to adjust and check their alignment, it was decided to align them individually and install them against a precision reference surface.

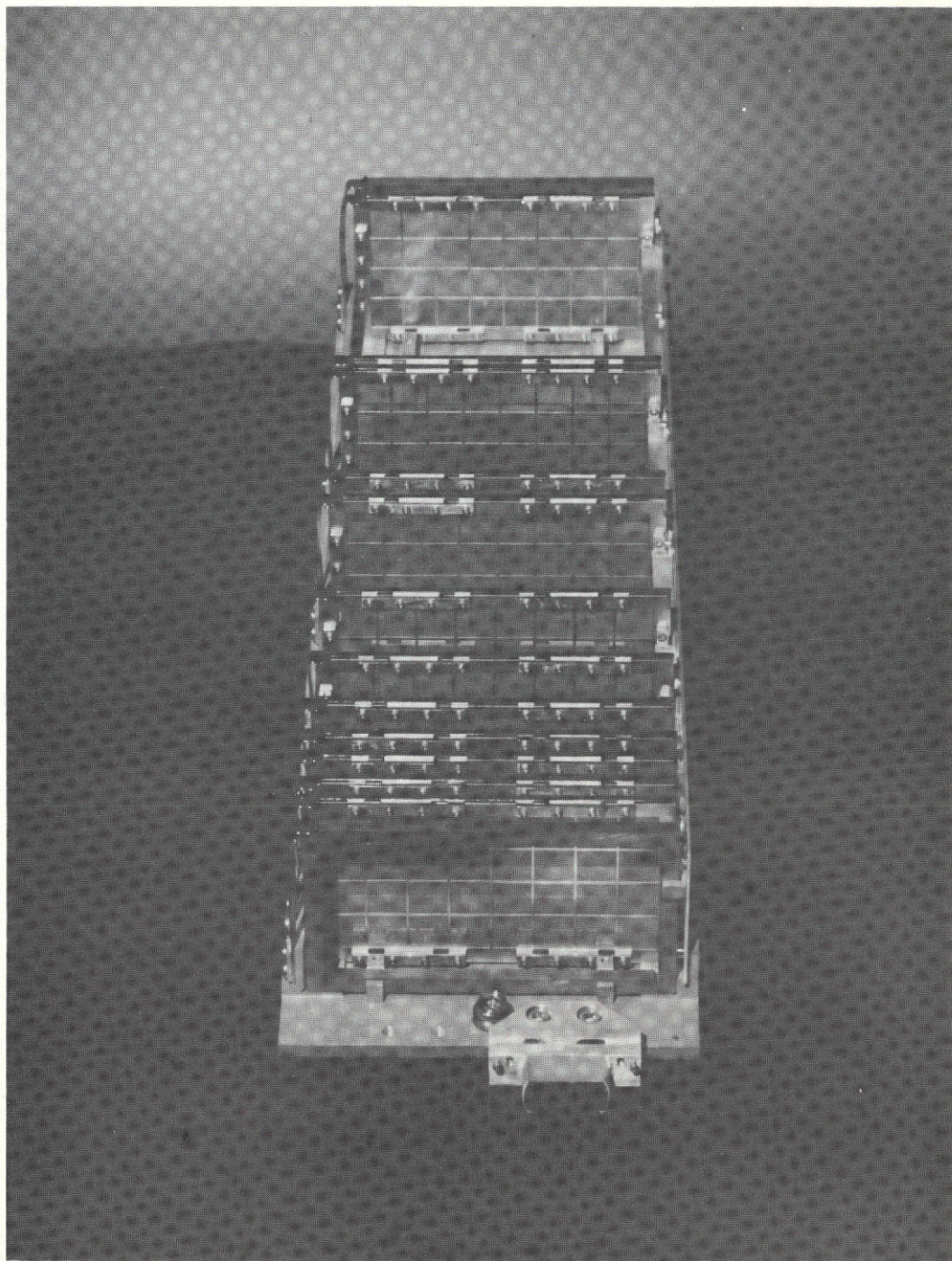


Figure 6. View of an X-ray Entrance Collimator with its Cover Removed

The main structural member is an aluminum channel whose critical inside surfaces are ground flat and straight. The channel is rough-machined, solution heat-treated, aged, finished-machined, hard-anodized, ground, and aged again to provide a smooth hard contact surface with dimensional stability. The reference surfaces were true to within 0.0003 in.

Each grid frame is held against the channel reference surfaces by a leaf spring that pushes diagonally across the frame. The frames are supported axially by loose-fitting slotted "combs" that also maintain the desired spacing between frames. The frames can be removed or otherwise disturbed and will snap back to their original position. Frames and springs are made of heat-treated beryllium copper. A very thin nickel plate is used for protection against corrosion.

The grids are clamped to the frames with their hole patterns the same distance from the edges of the frames to an accuracy of 0.00025 in. Assembly is facilitated by a fixture that mounts to the movable bed of a toolmaker's microscope. The grid pattern can be checked for parallelism with the frame edges and also for any distortion over the entire gride area.

An optically flat mirror was installed on each collimator to facilitate system alignment of the collimators.

C. EXPERIMENTAL MEASUREMENTS

Two major measurements were required for verification of the collimator performance: (1) the proper alignment of the grids had to be verified so that on-axis x rays could be passed and off-axis ones absorbed, (2) the x-ray axes of the collimators had to be found for proper experiment pointing. In the tests described herein, after crude verification that the collimators did transmit x rays, the x-ray axes were determined and then the transmission was measured.

Each of the three entrance collimators (two for the crystal spectrometers and one shared by the grating spectrometers) has a small adjustable mirror on its front end for alignment purposes. The purpose of the

alignment tests was to find the x-ray axis in relation to the normal to the mirror. The mirror could then be readjusted by using an autocollimator until the normal to the mirror coincided with the x-ray axis.

Initially, efforts were made to use the light from a helium-neon laser for alignment. This measurement was complicated by the diffraction of the beam by the collimator grids, but it was hoped that a strong diffraction maximum would be found when the beam and axis were properly aligned. Instead, the distribution of beam intensity versus angle was found to be bimodal. Since a detailed analysis of the diffraction by 12 closely spaced grids is extremely complex, this technique was abandoned.

A mechanical technique was also used in an effort to properly determine the x-ray axis. During the assembly of the collimators, the grid frames rest with one corner in a precisely machined right angle rail. The grid locations are all referred to this rail. Thus, the collimator axis should correspond precisely to the rail's longitudinal axis. In order to find the mechanical axis, an oblong gauge block with two long, precisely parallel faces was used. By using an autocollimator and marble flats and positioning the block successively on its long sides, the angle between the block end and the precisely parallel faces was found. Then, the gauge block was placed on one of its parallel sides against the collimator rail, and the angle between these two surfaces was measured by autocollimating on the block end and the alignment mirror. This gave the collimator axis referred to the mirror axis.

The method described above gave only marginally acceptable results. The collimator had to be partially disassembled for the measurement. Initially, the "comb" used to space the grid frames had to be removed to allow the gauge block to rest against the rail. It was feared that the removal of this part might affect the axis location. Therefore, one corner of the block was removed in order that the measurement could be made without removal of the comb. No significant change in the axis measurement resulted from this change.

The principal axis determination was made by using x-rays; the experimental arrangement is shown in Fig. 7. The measurement procedure was as follows. With all other components removed, the laser was aimed at the x-ray source aperture. The rear slit was then inserted and centered in the laser beam. The large mirror was inserted and adjusted until the laser beam autocollimated. An autocollimator was then used to coalign the collimator mirror with the large mirror, which was subsequently removed. The laser beam was then aligned with the collimator mirror normal. The table azimuth and elevation readings were recorded. Finally, the second slit was inserted and centered on the laser beam. The two slits thus defined an x-ray beam normal to the collimator reference mirror. The x-ray beam full width at half maximum was about 0.6 arc min, with a probable error in coaligning the x-ray beam and the normal to the mirror of 1 to 2 arc min. Note that the use of a slit results in an axis determination in only one dimension. For the other dimension, the procedure was repeated with the collimator mounted on its side in a special fixture.

The results of the x-ray alignment tests are given in Table 2. For each measurement, the difference between the x-ray axis and collimator reference mirror axis (angle offset) is given. Measurements taken after a single setup of the apparatus are bracketed. It is apparent that, even in the cases of multiple setups, the rms standard deviations were comparable to the error estimates given above. On the basis of the results shown in the table, the mirrors were adjusted such that there was no angular offset in the y direction for collimator 2, and none in the x direction for collimators 2 and 3. Since the other axes were within 1 arc min of the x-ray axis, no adjustment was made in these directions.

The second important measurement was a check of the collimator transmission for verification of the accuracy of assembly. Initially, the tests were performed in air following the procedure described below. However, the results were unsatisfactory because, in air, high-energy x rays

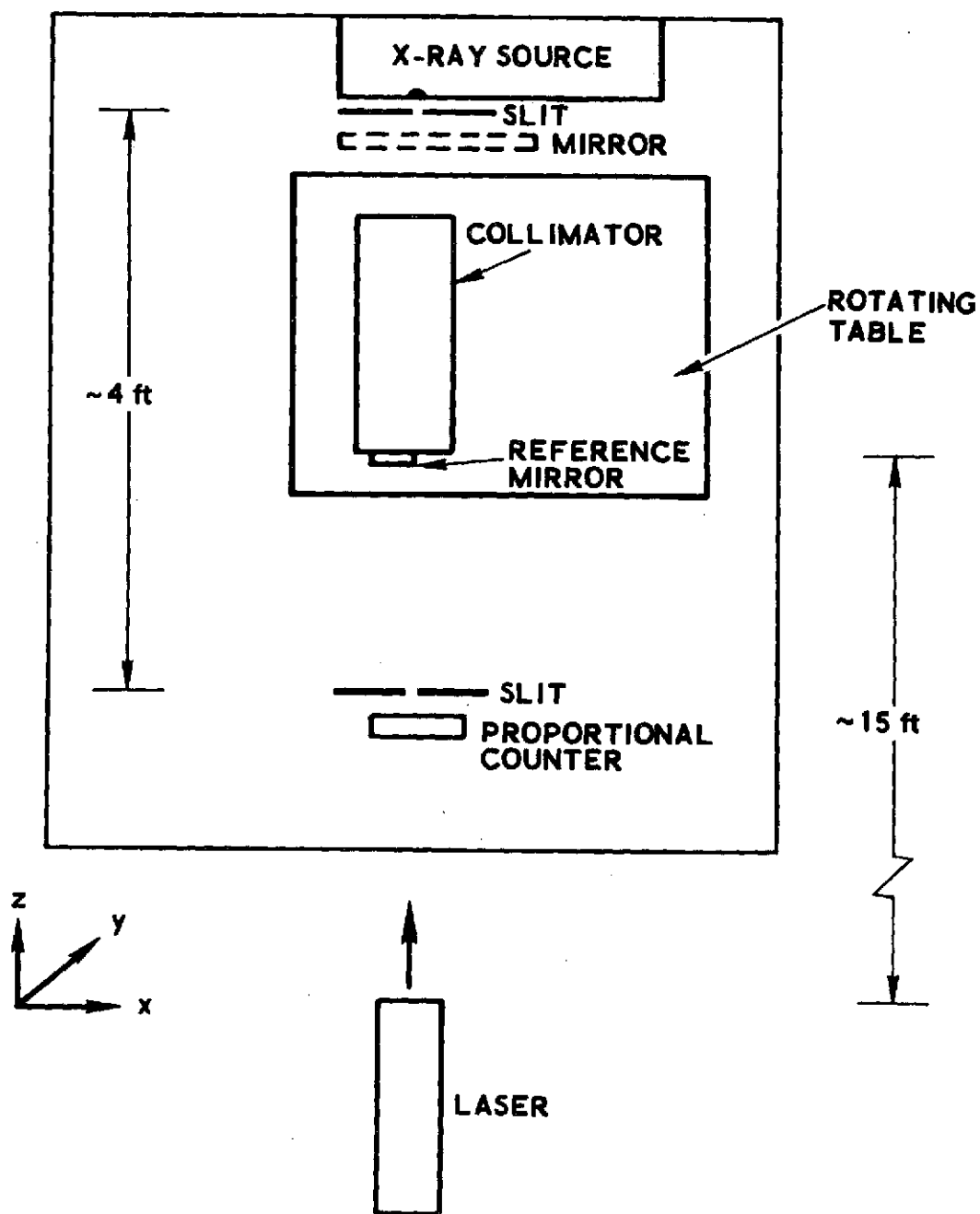


Figure 7. Experimental Arrangement for the X-ray Collimator Principal Axis Determination

Table 2. Results of X-ray Alignment Tests

Collimator No.	Direction	Angle Offset arc min., arc sec.	rms Uncertainty (σ), standard deviation
1	y	+1'30"	0"
		+1'30"	
	x	-1'37"	1'01"
		-1'42"	
		-1'17"	
		+0'21"	
		+0'21"	
		+0'45"	
		+0'30"	
2	y	+1'03"	0'11"
		+0'40"	
		+0'40"	
	x	+2'54"	
		+3'03"	
		+3'09"	
		+2'13"	0'49"
		+2'18"	
		+3'05"	
		+3'20"	
		+1'07"	
		+1'07"	
3	y	-0'27"	0'02"
		-0'30"	
		-0'32"	
	x	+2'57"	0'13"
		+3'23"	
		+2'51"	
		+2'51"	

had to be used, and even a small transmission through the opaque part of the grids could yield a substantial error in the measurements. Therefore, the final transmission tests were performed in vacuum.

The measurement apparatus for the x-ray transmission tests is shown in Fig. 8. The collimator being tested could be rotated about x and z axes and translated along the x axis by using the lead screw from outside the vacuum chamber. The aperture that contained the 30-arc-min collimator could be translated along the x or z axes. The x-ray source permitted easy removal for the initial alignment or for changing anodes.

Because of the ample provisions in the experimental arrangement for adjustability, only a crude initial alignment was required. This was done as follows. The laser and the 30-arc-min precollimator were aligned with the center of the proportional counter such that the laser beam passed through a region that was readily available to the collimator to be tested. The geometry was then such that all x rays that passed through the precollimator would strike the proportional counter window when the test collimator was translated out of the beam. The 30-arc-min precollimator was then removed, and the test collimator was translated into the laser beam and adjusted in azimuth and elevation until the laser beam was reflected from the collimator mirror and autocollimated. The 30 arc-min precollimator was then inserted and its proper alignment with the laser beam reverified. Finally, the x-ray source was mounted and the chamber pumped out for the test.

The test consisted of measuring the x-ray flux at the proportional counter with the test collimator in and out of the beam. Because the precollimator had a conical angular response with half-angle of 30 arc min ($= \pi/360$), the flux with the test collimator out was

$$F_o = \int C_p I_o(\Omega) T(\theta) d\Omega dA$$

where C_p is the precollimator transmission, and $T(\theta)$ is its angular response.

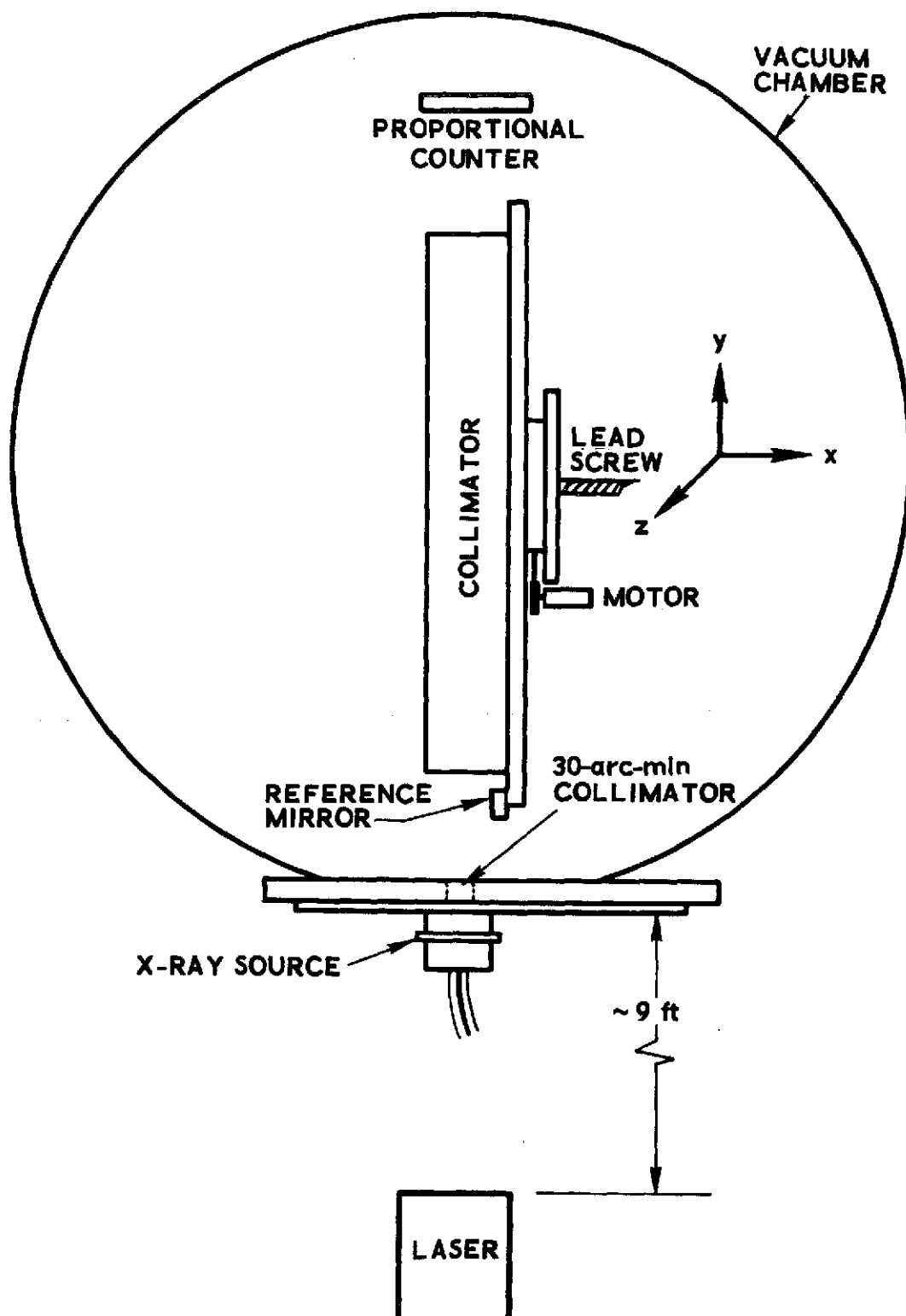


Figure 8. Experiment Arrangement for the X-ray Transmission Measurements

Since the beam width is only 30 arc min, $I_o(\theta)$, the source intensity, may be assumed to be constant as a function of angle θ . Thus, recalling that $T(\theta)$ is a triangular function, we can write the integral as

$$F_o = I_o C_p \int_0^{\pi/360} \left(1 - \frac{360}{\pi} \theta\right) 2\pi\theta d\theta dA$$

$$= \frac{\pi}{3} C_p I_o A \left(\frac{\pi}{360}\right)^2$$

Similarly, with the test collimator in place,

$$F = C_p I_o A C \int_{\Omega} d\Omega' T'(\theta, \phi)$$

where the same assumptions as before are made with respect to the constancy of the source intensity I_o , C is the collimator transmission, and T' is the collimator angular response. Since the angles considered are very small, we may write, with angles α and β measured along the x and y axes, respectively,

$$d\Omega' = d\alpha \cdot d\beta$$

It can be shown that the angular response function can be written as

$$T' = T'_x(\alpha) \cdot T'_y(\beta)$$

where the x and y angular response function are triangular with maximum angles α_o and β_o of 83 and 123 arc sec, respectively, i.e.,

$$T' = \left(1 - \frac{\alpha}{\alpha_o}\right) \cdot \left(1 - \frac{\beta}{\beta_o}\right)$$

and

$$\int_{\Omega} T' d\Omega' = \int_{-\alpha_o}^{+\alpha_o} \int_{-\beta_o}^{+\beta_o} \left(1 - \frac{\alpha'}{\alpha_o}\right) \left(1 - \frac{\beta'}{\beta_o}\right) d\alpha' d\beta'$$

Performing the straightforward integration yields

$$F = C_p C I_o A (5.96 \times 10^{-4})(3.98 \times 10^{-4})$$

where the angles in arc seconds have been converted to radians. Thus, the final ratio of the flux with the collimator in and out is

$$\frac{F}{F_o} = 2.98 \times 10^{-3} C$$

where C is the on-axis transmission of the collimator and, from geometrical considerations, assuming perfect alignment, is expected to be 0.44.

The measured average values of C for each of the three collimators are given in Table 3 together with the rms standard deviation (σ) for each set of collimator measurements.

Table 3. Measured Effective Values of Collimator Transmission Factor

Collimator No.	No. Measurements	C _{average}	σ
1	13	0.287	0.053
2	12	0.437	0.027
3	11	0.506	0.029

Each collimator transmission was obtained with at least two different sets of measurements by using electronics with different dead times. The results for collimators 2 and 3 were in reasonable agreement with the predicted C values, and the standard deviations were reasonable. The results for collimator 1 indicated a probable grid misalignment. Three separate sets of measurements were made on collimator 1, and the reproducibility of the results was poor.

Because the grating spectrometer was considered to be the most speculative instrument on the rocket, collimator 1 was used with it; collimator 2 was used with the RAP crystal spectrometer, and collimator 3 with the ADP crystal spectrometer.

D. COLLIMATOR ALIGNMENT WITH THE SOLAR ASPECT SYSTEM (SPARCS)

A 10-in. half-moon mirror was mounted on a subplate and supported with three adjustable standoffs in a position perpendicular to the payload roll axis. This mirror served as a secondary reference surface and was mounted such that it could be viewed simultaneously with the SPARCS mirror or the collimator alignment mirror by using a 3-in. autocollimator.

The first step in the procedure was to adjust the plane of the secondary reference mirror such that it was parallel with the plane of the fixed SPARCS eyes. This was done by adjusting the three standoffs of the reference mirror until the reticle images from the SPARCS eyes and the reference mirror overlapped exactly when viewed through the autocollimator.

Each of the collimators was then moved about in an x-y viewing plane until the reference mirrors on the collimators were parallel with the plane of the secondary reference mirror, as indicated by the autocollimator images. The alignment mirrors of the collimators, the secondary reference mirror, and SPARCS eyes were then coaligned.

E. GRATING EXIT COLLIMATOR DESCRIPTION

The equation

$$m\lambda = a(\sin \alpha + \sin \beta)$$

locates the angles β of diffraction maxima if the incident radiation makes an angle α with respect to the normal to a flat diffraction grating. In the equation, a is the grating groove spacing, and m is the order number. It is evident that the reflected radiation and the incident radiation must be collimated for grating spectroscopy to be effective. Accordingly, each of the two grating spectrometers was equipped with a mechanical exit collimator.

The exit collimators, like the entrance collimators, are of modified McGrath design. Since collimation is required only along the dispersion direction, the grid slots are much narrower along the direction of dispersion than normal to the dispersion direction. The collimators are 8.2 in. long, and the narrow grid slot size is 0.006 in. Thus, the angular resolution was 151 arc sec (FWHM). The limit on spectral resolution, placed by both collimators, was

$$\Delta\lambda = ma(\cos \alpha \Delta\alpha + \cos \beta \Delta\beta)$$

where $\Delta\alpha = 82$ arc sec and $\Delta\beta = 151$ arc sec.

Since the grating spectrometer operates by holding the grating fixed (α constant) and scanning the collimator to vary β , a precise alignment is not necessary for the exit collimator. The wavelength reference is obtained from a known strong line and the known scanning rate of the collimator. Thus, only a measurement of the transmission is required. This transmission measurement on the exit collimators followed the same procedure as that described earlier for the entrance collimators. However, the calculation of the transmitted flux is slightly different because the collimation is effective in only one dimension.

F. ENTRANCE COLLIMATOR MOUNTING

Each of the main collimators is mounted to the "I" beam web by a three-point attachment on the base channel of the collimator. Washers are used as spacers to prevent contact at any other location, and shims are used to adjust the tilt of the mounting plane. Oversize screw holes permit adjustment in the mounting plane. Spherical washers under the screw heads prevent transmitting stresses. This mounting method is satisfactory as long as the structure is not deflected by external loading or by temperature differences. The more exotic system used for the exit collimators was not easily applied nor was it considered necessary.

G. GRATING EXIT COLLIMATOR MOUNTING

A superior mounting system was used for the exit collimators in the grating drive because it was an easily accomplished and correct principle, not because of a demonstrated need. In the three-point kinematic attachment, the collimator body is rigidly held in three translational and three rotational directions, both positive and negative; a dimensional change between the attach points, e. g., by thermal expansion, will have minimal effect.

The structure near the attach points is arranged such that it has high or low spring rates in the various directions. Because the low-rate directions (soft springs) can exert only minimal forces when displaced, they do not affect the collimator. The attach points have minimum contact area, and spherical washers are used to prevent local moments when the screws are tightened.

VI. DETECTOR SYSTEMS

A. INTRODUCTION

Gas flow proportional counters are used as the photoelectric detectors for both the crystal and grating spectrometers. Each crystal and grating has its own counter; there are a total four flow counters. The counters are all rectangular, with an entrance aperture of 5×10 cm. The physical dimensions of all four flow counters are identical. Each counter has its own control and data processing circuitry with essential data outputs telemetered on separate IRIG channels. Basic detector electronics consist of a counter gas pressure regulator, a high-voltage supply, and detector event scalers. Two separate gas sources are available to supply gas to each detector's regulator depending on the type of gas required. The gases used are a mixture of 90% Ar, 10% CH₄ (P-10 gas) and a mixture of 65% Ar, 25% Xe, and 10% CH₄. Counter window material, counter gain, gas type, and gas pressure are the variables used to tailor the detector for a specific x-ray or EUV wavelength region. The flight parameters and the wavelength regions covered by each detector are given in Table 4.

Table 4. Rocket Detector System Parameters

Wavelength Interval, Å	Window Material	Gas Type	Gas Pressure, mm	Flight Counter Gain
1-10	Kimfoil	65% Ar, 25% Xe, 10% CH ₄	760	1,500
5-26	Polypropylene	65% Ar, 25% X3, 10% CH ₄	760	3,300
20-120	Polypropylene	90% Ar, 10% CH ₄	180	10,500
100-500	Polypropylene	90% Ar, 10% CH ₄	180	18,600

PRECEDING PAGE BLANK NOT FILMED

B. FLOW PROPORTIONAL COUNTER CONSTRUCTION

The detectors are constructed of nickel-plated brass with a rectangular internal geometry of $1.25 \times 5.05 \times 11.15$ cm. This internal geometry is divided by thin nickel sheets into four adjacent detecting cells, each with a separate anode wire and $1.25 \times 1.26 \times 11.15$ cm in dimension. Detector gas flow ports are positioned such that gas flows serially the length of each cell. The cells are electrically coupled such that a single high-voltage supply and signal detection electronics serve all four cells of each detector. A detector front plate, which acts as a "strongback" for the grid/window combinations, seals the detector entrance by means of an O-ring. The grid structure, which is on the outer side of the window, supports the window only if the counter internal pressure is greater than the external pressure. Transmission of the supporting grid is 56.83 percent.

C. DETECTOR WINDOW PROPERTIES

The detector windows are constructed of commercially available Kimfoil ($C_{16}H_{14}O_3$) and carbon-coated polypropylene (CH_2). The Kimfoil comes with a coating of aluminum approximately $400\text{-}\text{\AA}$ thick. Since the walls of the counters are photosensitive, the windows are coated with the Aquadag or aluminum in order to exclude visible light. The Kimfoil and polypropylene are cemented to a support grid. In both cases, the window material was cemented to the grid so that the film's electrically conductive coat would be part of the counter's interior. All window transmission measurements included the support grid.

Transmission measurements were made by using a single Bragg crystal spectrometer to accurately define the wavelength of the x-ray beam. Measurements were made at 8.34, 9.89, 13.3, 15.97, and $18.3\text{ }\text{\AA}$. For each wavelength, the window transmission was measured at three different locations on the window surface for each of the flight counters. A best fit to the transmission data taken at the five wavelengths was made by using Henke's mass absorption coefficients and the known transmission of the support grid. In this way, an effective window thickness was determined.

The transmission at any wavelength could be determined by using a table of mass absorption coefficients and the measured effective thickness (g/cm^2) of each window. The effective thicknesses of the flight windows are given in Table 5.

Table 5. Detector Window Effective Thicknesses

Detector	Window Material	Effective Thickness, g cm^{-2}
RAP crystal spectrometer	Polypropylene	1.55×10^{-4}
ADP crystal spectrometer	Kimfoil	2.55×10^{-4}
Short λ grating spectrometer	Polypropylene	1.41×10^{-4}
Long λ grating spectrometer	Polypropylene	1.30×10^{-4}

A typical measured window transmission (including the supporting grid) is given in Fig. 9.

The gas pressures were 760 mm of Hg for the crystal spectrometer detectors and 180 mm of Hg for the grating spectrometer. These pressures were selected for several reasons: one was to maximize the gas absorption efficiency of the counters. Over the wavelength region of 2 to 25 \AA , it was experimentally shown that 1 atm of 65% Ar, 25% Xe, and 10% CH_4 gas in the detector provided sufficient absorption. Over the region of 20 to 500 \AA for the gratings, a counter pressure of 100 mm of P-10 gas provided a similar effect. The final choice of 180 mm for the grating detectors was based on counter gain versus high-voltage sensitivity considerations. At 180 mm of pressure, the absorption efficiency for a photon of wavelength 20 \AA is 99.5 percent; of course, it is 100 percent for all longer wavelengths.

The argon, xenon, methane mixture at 1 atm in the crystal spectrometer detector was chosen to give adequate absorption throughout the wavelength range of interest (3-25 \AA). The reason for the several components was to "fill in" lack of absorbing power near absorption edges of a particular component. The absorption coefficient of argon drops sharply above the K

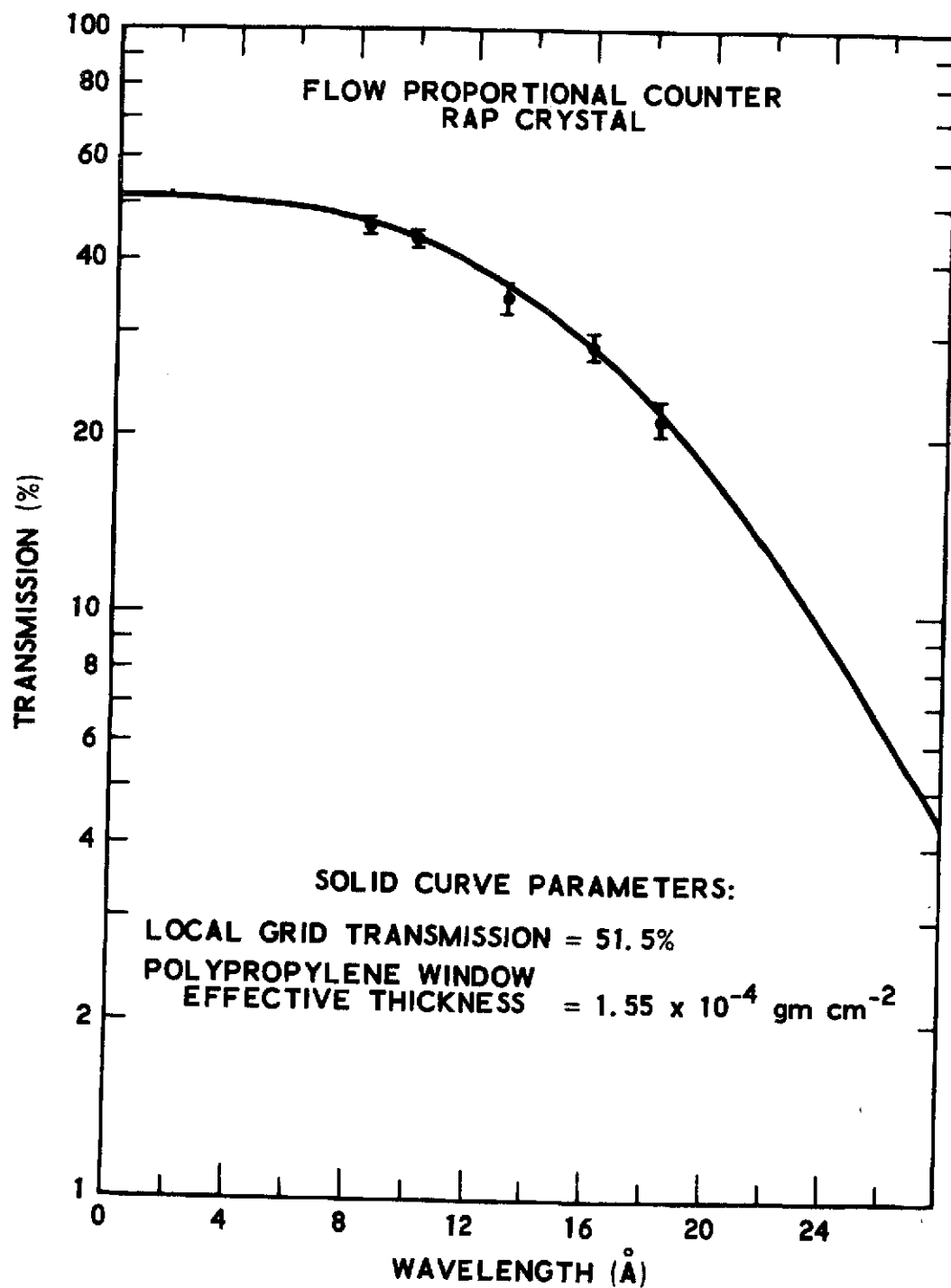


Figure 9. X-ray Spectrometer Detector Window/Grid Transmission Measurements vs Wavelength

absorption edge at 3.9 \AA . The xenon increases the efficiency in this wavelength range and at wavelengths below its L absorption edge at 2.6 \AA . Furthermore, it prevents the loss of photopeak counts because of the escape of argon K shell radiation following photoelectric absorption of incident x rays. The gas absorption efficiency for this detector is shown in Fig. 10. It is evident that, beyond 8 \AA , the absorption efficiency is essentially 100 percent.

Detector efficiency is simply the product of window transmission and gas absorption efficiency. In the case of the P-10 gas used for the grating spectrometers, detector efficiency is only the window transmission because the gas absorption efficiency is 100 percent over the entire wavelength range of interest. For the crystal spectrometer, counter gas absorption efficiency significantly affects overall counter efficiency below 6 \AA ; above 8 \AA , the efficiency is totally dictated by the window transmission.

Tests of detector gain versus pressure were performed in order to optimize pressure setting after the effect of gas absorption detector efficiency was considered. Tests were run at 2, 8.3, and 44 \AA for a number of pressures between 70 and 760 mm of Hg. P-10 gas was used in these tests. Counter gain was obtained by using a 400-channel pulse height analyzer. Some of the results of these measurements are shown in Fig. 11.

D. RISE-TIME DISCRIMINATION

In order to minimize background for both the crystal and grating spectrometers, rise-time discrimination was provided. A high-energy charged particle leaves a long ionized track throughout the detector upon traversing the detector, whereas an EUV or x-ray photon is primarily absorbed by the photoelectric effect at a single point in the detector. Primary low-energy electrons and photons are produced at this point and are confined to a small volume as a result of their short range in the gas. Hence, the rise time for a pulse from a charged particle traversing the detector is longer than that from a photon absorption event in the detector.

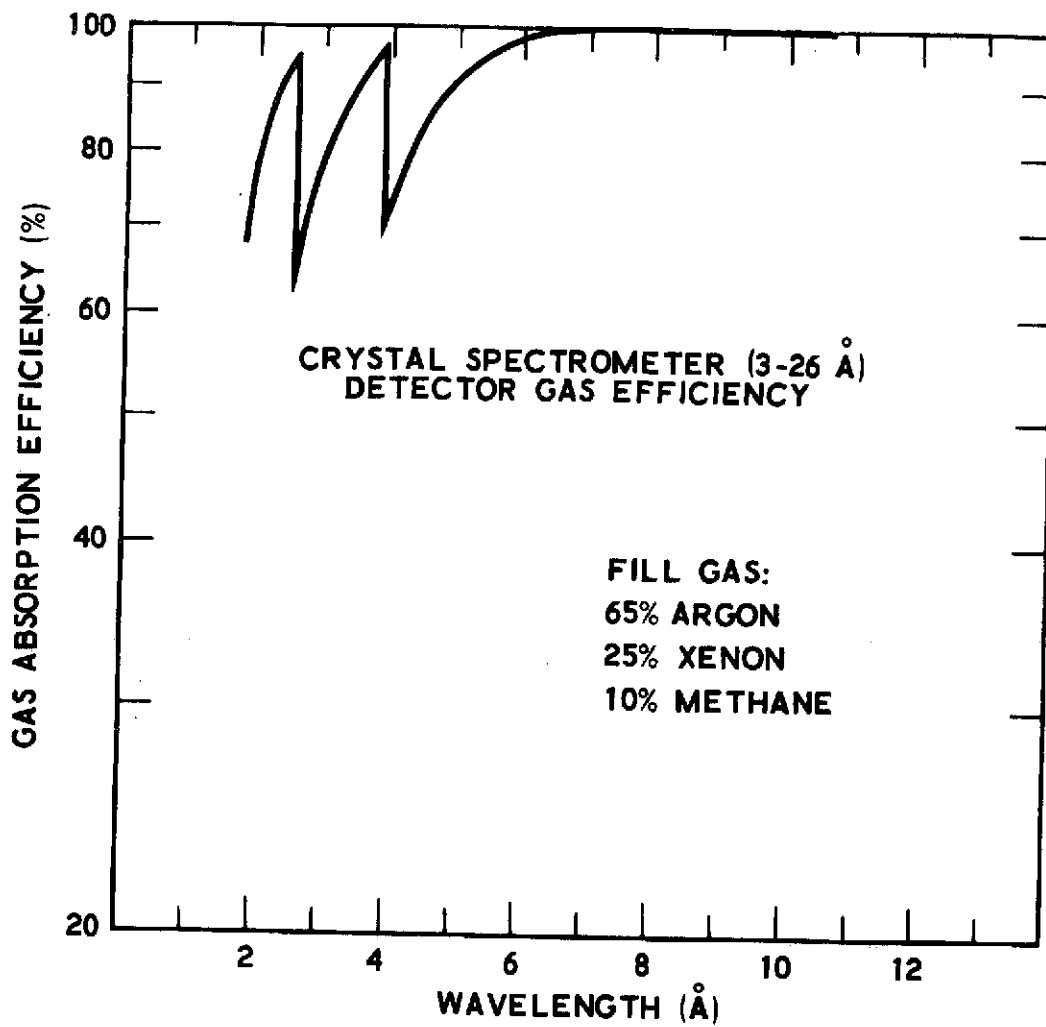


Figure 10. X-ray Spectrometer Detector Gas Absorption Efficiency vs Wavelength

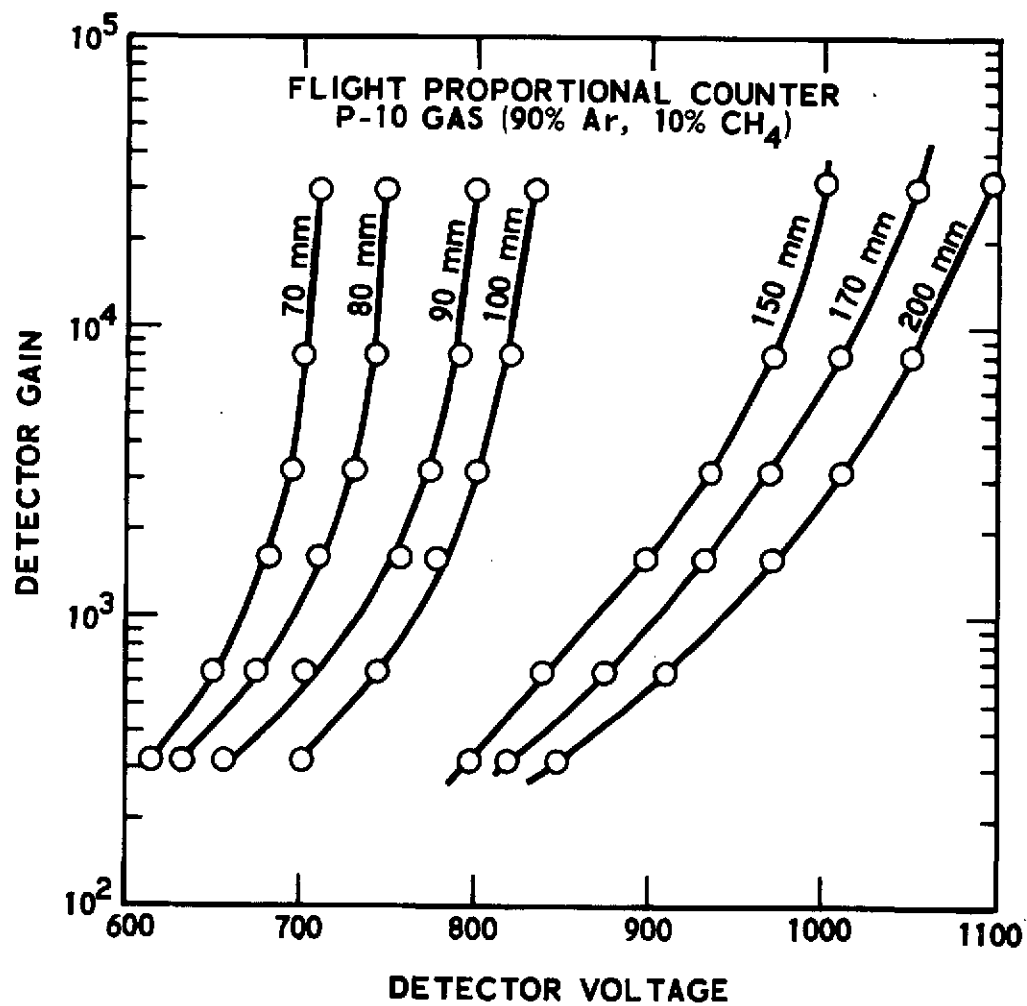


Figure 11. Grating Spectrometer Detector Gain vs Applied High-Voltage for a Number of Internal Gas Pressures

Rise-time measurements in the spectrometer detectors were made at the same time as the gain-pressure measurements. The rise-time discriminator used in these measurements is the same discriminator used during the rocket flight. The discriminator segregates detector events according to event rise time. For a given rise time, the discriminator accumulates all events with rise time less than or equal to the discrimination time as well as all events with longer rise time.

Four sets of rise-time data were taken with P-10 gas. There are two different families of data. First the pressure was varied from 70 to 760 mm. At each pressure, four samples of rise-time data for a Fe^{55} x-ray source (2 \AA) were recorded. These data (Table 6) indicate a slightly better performance for the discriminator for pressures between 200 and 400 mm. The second family of data for the P-10 gas were obtained by fixing counter pressure at 180 mm and varying wavelength. The wavelengths used were 8.3, 17, and 44 \AA , and a Co^{60} source to simulate charged particles. These data are tabulated in Table 7. The rise-time data between 2.54 and 17 \AA are all essentially similar. However, at 44 \AA , rise-time discrimination does not have the same background rejection potential.

The last two sets of data were obtained at 760 mm with the same test except that two different counters were used. The flight counters were used in these tests. For both gases, rise-time data for a Fe^{55} source (2 \AA) are compared with that for a Co^{60} source.

This comparison data appear in Figs. 12 and 13. The data show a 5:1 rejection of background (Co^{60}), with only a 5 percent loss of signal if a discrimination time of 100 nsec is chosen for the Ar, Xe, CH_4 gas and 85 nsec for the Ar, CH_4 gas.

E. DETECTION ELECTRONICS

Flow counter electronics (Fig. 14) are independent for each of the flow counters, except for circuit power and gas regulation, which are shared. Each flow counter has three signal outputs. The data are segregated by means of signal magnitude and signal rise time. Segregation by means of

Table 6. Rise-Time Discrimination vs Pressure Data Taken at 2Å

	τ , ns	760 mm	400 mm	200 mm	170 mm	150 mm	100 mm	90 mm	80 mm	70 mm
Gain = 320	100	0.627	0.575	0.655	0.446	0.390	0.379	0.354	0.307	0.217
	125	0.929	0.974	0.973	0.934	0.920	0.865	0.873	0.815	0.763
	140	0.981	0.990	0.985	0.982	0.972	0.964	0.964	0.922	0.918
	160	0.992	0.996	0.993	0.989	0.986	0.977	0.986	0.969	0.966
Gain = 640	100	0.700	0.830	0.859	0.576	0.493	0.417	0.385	0.247	0.113
	125	0.977	0.988	0.974	0.959	0.930	0.917	0.886	0.839	0.774
	140	0.983	0.994	0.989	0.982	0.986	0.970	0.965	0.958	0.917
	160	0.987	0.996	0.993	0.989	0.992	0.989	0.983	0.976	0.966
Gain = 1600	100	0.920	0.967	0.915	0.676	0.567	0.280	0.130	0.073	0.050
	125	0.978	0.987	0.987	0.973	0.959	0.897	0.820	0.803	0.600
	140	0.882	0.990	0.994	0.939	0.981	0.979	0.960	0.960	0.909
	160	0.984	0.996	0.997	0.992	0.990	0.981	0.983	0.976	0.965

Table 7. Rise Time Discrimination vs Wavelength Data Obtained at a Pressure of 180 mm of Hg

Gain = 160	τ , ns	Fe ⁵⁵ 2.0 Å	Al _{Kα} 8 Å	Fe _{Kα} 17 Å	C _{Kα} 44 Å	Co ⁶⁰	Cosmic Rays
	50	0.002	0.007	0.005	0.032	0.006	0.009
	75	0.008	0.020	0.017	0.183	0.036	0.031
	94	0.509	0.671	0.661	0.472	0.116	0.113
	100	0.918	0.979	0.964	0.673	0.217	0.232
	125	0.982	0.995	0.989	0.861	0.479	0.493
	140	0.992	0.995	0.994	0.933	0.660	0.674
	160	0.997	0.997	0.995	0.963	0.775	0.815

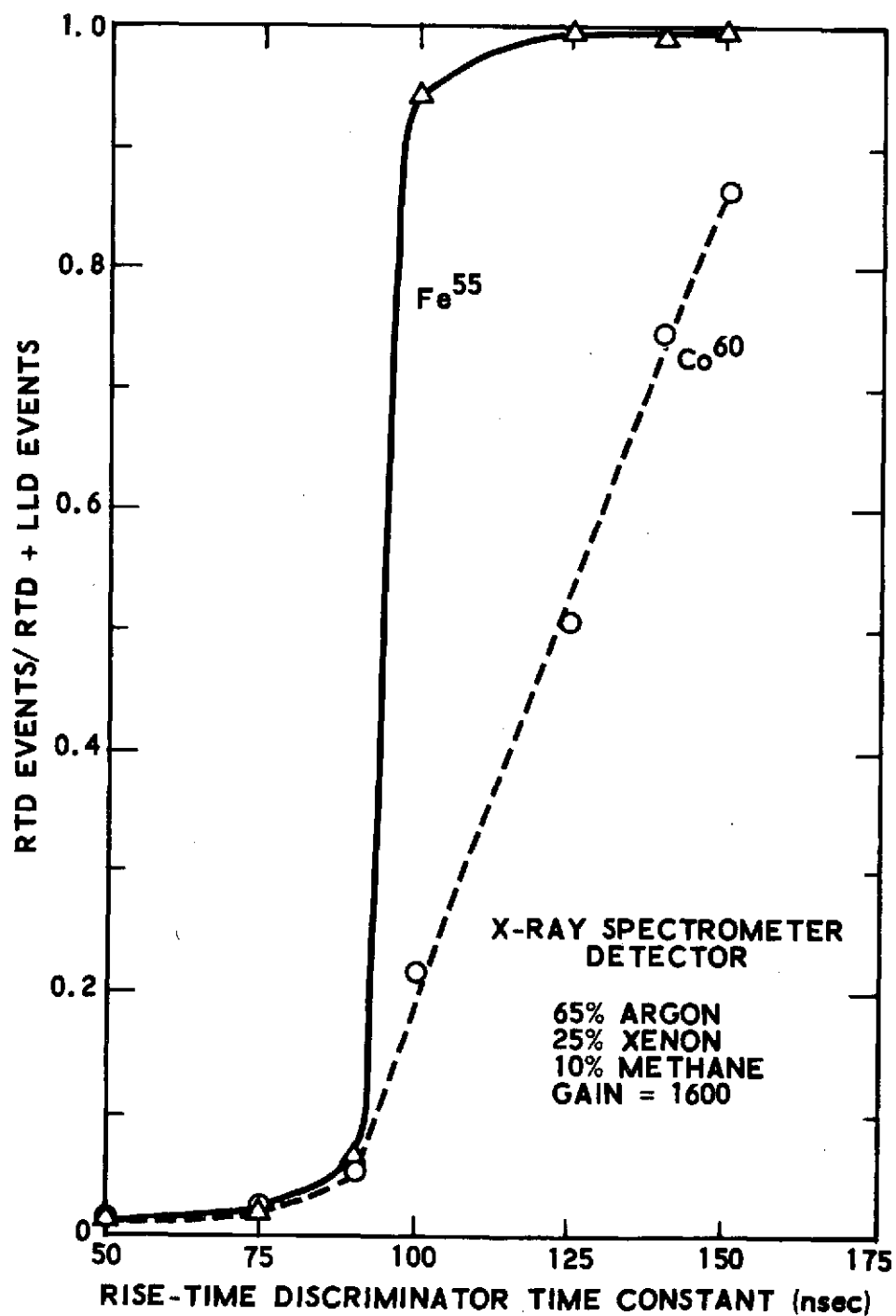


Figure 12. Efficiency of Detection of X rays (Fe^{55} source) and Charged Particles (Co^{60} source) vs Rise-Time Discrimination Circuit Time Constant for an Argon, Xenon, Methane Filled Detector.

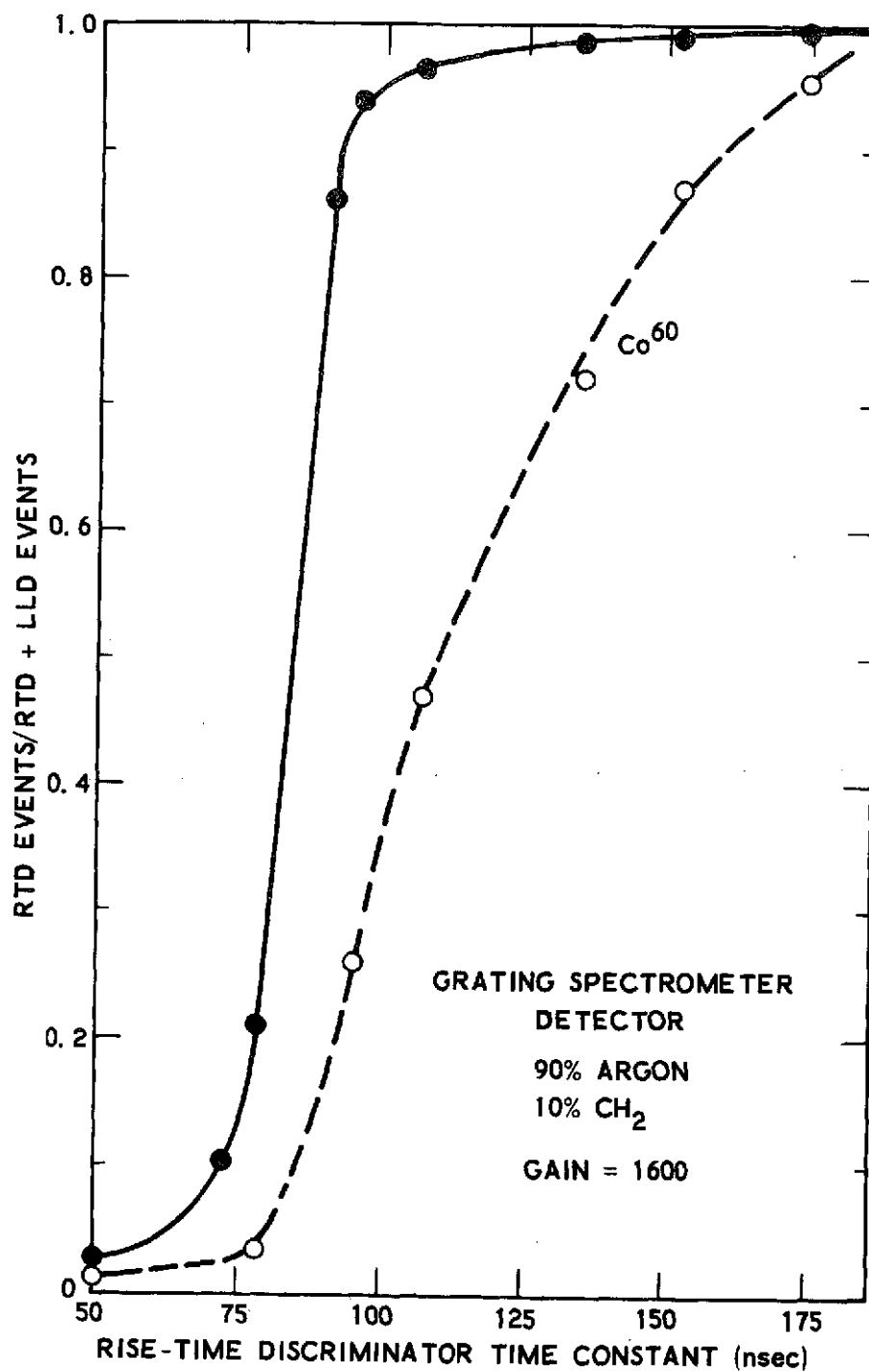


Figure 13. Efficiency of Detection of X rays (Fe^{55} source) and Charged Particles (Co^{60} source) vs Rise Time Discrimination Circuit Time Constant for the Grating Spectrometer and an Argon, Methane (P-10 gas) Filled Detector

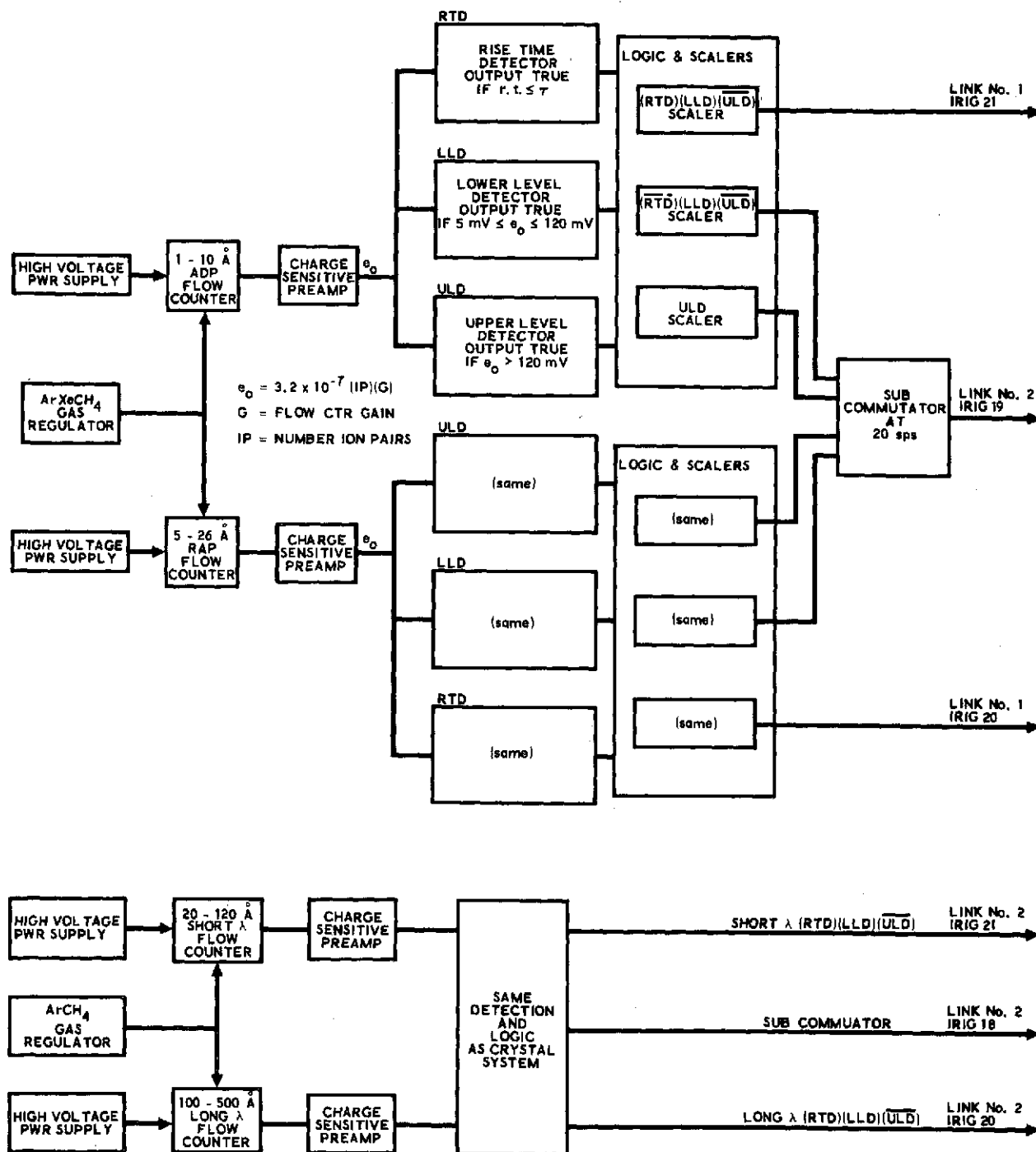


Figure 14. Block Diagram of Flow Proportional Counter Electronics

signal magnitude is accomplished with lower level (LLD) and upper level (ULD) detectors. These voltage thresholds are the same for all four flow counters. Threshold values at the charge amplifier output are 5 mV for the lower threshold and 120 mV for the upper threshold. Lower-level data consist of those events with magnitude between the ranges of 5 and 120 mV. These correspond to real x-ray and XUV events. Upper-level data are those detector events with magnitude that equals or exceeds 120 mV. These events are, presumably, charged particles or other background. A rise-time discriminator subdivides low-level detected events as a function of signal rise time. All lower-level detector signals with rise time less than or equal to the threshold value were called rise-time discriminated data (RTD) and satisfy the condition for real x-ray and XUV events. Those lower-level detected signals with rise time greater than the threshold are also called LLD, but are excluded from rise time considerations, i.e., not RTD, because they are presumably charged particles.

The RTD data are monitored on an open IRIG channel. The LLD and ULD data for both crystal detectors, a total of four data points, were each sampled five times per second. Grating spectrometer data were monitored in the same way.

1. RISE-TIME DISCRIMINATOR AND THRESHOLD DETECTOR

The rise-time discriminator separates the lower-level detected data by the rise-time characteristics of the events signal. These signals are accumulated in two different digital counters. Digital counter outputs are converted into analog signals for telemetry purposes. The upper-level signal is handled in the same way. A 960-counts-per-sec signal uniformly distributed in time would result in an apparent 30 Hz sawtooth waveform at the accumulator's output. The fine structure of the sawtooth ramp consists of 32 discrete steps of 160 mV each.

Threshold detection is accomplished by means of a standard comparator whose response time is less than 100 ns. Rise-time detection converts the event's signal rise time into a pulse magnitude. This rise time pulse

magnitude is inversely related to the detector event's length of rise time. Differentiation of the detector event results in a new signal with a magnitude inversely proportional to rise time. The technique actually used is similar to differentiation. The resultant detected signal is

$$e_{\text{det}} = e_o(t) - e_o(t + \tau)$$

The variable (τ) is changed in order to change the rise-time threshold. This rise-time signal is then threshold-detected. Depending upon the threshold chosen, events with rise times less than or equal to the threshold are detected and accumulated.

2. HIGH-VOLTAGE SUPPLIES

The voltage supply is a standard regulator inverter section driving Cockcroft Walton voltage doubling circuitry. Regulation as a function of temperature and regulation stability for this particular supply are both extremely good. A significant effort was directed toward the design of the regulator because of the counter's gain sensitivity as a function of voltage. The high-voltage supply temperature regulation at 1500 V is ± 1.5 V, for a 50°C change at about room temperature. Stability is better than 1 V. Flow counter gain is adjusted by means of the high-voltage supply.

3. HOUSEKEEPING ELECTRONICS

Monitoring of spectrometer positions and rate, circuitry supply voltages, temperatures, counter gas pressures, and camera exposure time (Section VII) can be combined and are called housekeeping circuitry. Verification of the flight programmer sequence is also derived from this same monitoring circuitry.

Spectrometer position is monitored by means of both limit switches and a potentiometer. Spectrometer rate is a measure of the stepper motor's local oscillator frequency. The local oscillator output is accumulated in a digital counter and digital-to-analog converted. The analog output is a sawtooth with a leading edge that is a ramp of 128 steps of 40 mV each. The

potentiometer is directly coupled to the spectrometer output drive shaft. The spectrometer motion is terminated at a mechanical stop, located at either extreme of the detector travel. The leading edge of this stop is a microswitch that is actuated when the spectrometer detector reaches the stop. This microswitch is part of the spectrometer drive control. Both the crystal and grating spectrometer drives have identical control and housekeeping circuitry. The crystal mechanism is a θ - 2θ mechanism, i.e., both the crystals and detectors move. In the case of the grating spectrometer, only the detectors move. The gear ratio, angular step size, and step rate (local oscillator) for the spectrometers are as follows:

<u>Gear Ratio</u>	<u>Angular Step Size</u>	<u>Local Oscillator</u>	<u>Detector Total Travel</u>
Grating, 64,200/1	5.046 arc sec/step	76.5 Hz	10.73°
Crystal, 6880/1	23.5 arc sec/step	91.73 Hz	120.0°

F. FLOW GAS CONTROL SYSTEM

1. GRATING SPECTROMETER CONTROL GAS SYSTEM

The function of the grating spectrometer gas control system (GSGCS) is to supply a gas mixture of 10 percent methane and 90 percent argon (P-10 gas) to the grating spectrometer's two flow proportional counters during the prelaunch, ascent, and active measurement phases of the rocket's flight.

During the prelaunch phase, the GSGCS is active several hours prior to launch to permit a system checkout and to purge the flow counters of contaminants and moisture. External gas is supplied to the GSGCS through an umbilical in order to conserve the onboard gas supply.

The longer wavelengths of the radiation analyzed by the grating spectrometer dictated that thin (and therefore fragile) flow counter windows would be required. Thus, the GSGCS might have to support a wide range of window leak rates.

Since pulse height discrimination was used in the detection system, the counter gains had to be reasonably constant and sufficiently high to compensate for the low-energy loss in the detectors at these longer wavelengths. Therefore, counter pressure had to be low and accurately controlled during the active measurement phase of the flight. Also, a reasonably well-controlled differential pressure across the windows was necessary during the rocket's ascent because of their fragile nature. In the event of a total or catastrophic failure of a window of one counter, the GSGCS was also to continue supplying gas to the remaining counter in order that it would not be affected by the failure. It was therefore necessary that the GSGCS have a failure detection and automatic shut-down capability in order to conserve the onboard gas supply.

A block diagram of the GSGCS is shown in Fig. 15. The onboard gas is supplied by a high-pressure cylinder located in the aft section of the experiment payload. The gas handling hardware in the aft section is shown in Fig. 16. The supply capacity at the time of launch is about 0.41 standard cubic feet (SCF) at a pressure of 1800 psi. A high-pressure gauge is provided as a visual monitor during prelaunch activities and is observable through an access hatch in the aft section of the payload.

The gas is reduced to 7 psi (absolute) with a mechanical absolute pressure regulator. It is then passed through a precision isolation (check) valve to protect the regulator from back pressure prior to launch. The ground-supplied gas is connected to the GSGCS at this point and supplied at a pressure of 25 psi through another precision isolation valve and an umbilical disconnect fitting.

The umbilical disconnect fitting contains a Schrader valve that automatically closes at launch. The isolation valve provides redundancy to ensure a tight seal to the system.

The P-10 gas is passed through the bulkhead into the forward section of the payload. It is then split into two identical paths, each of which services an individual flow counter. Within each path, the gas is first fed

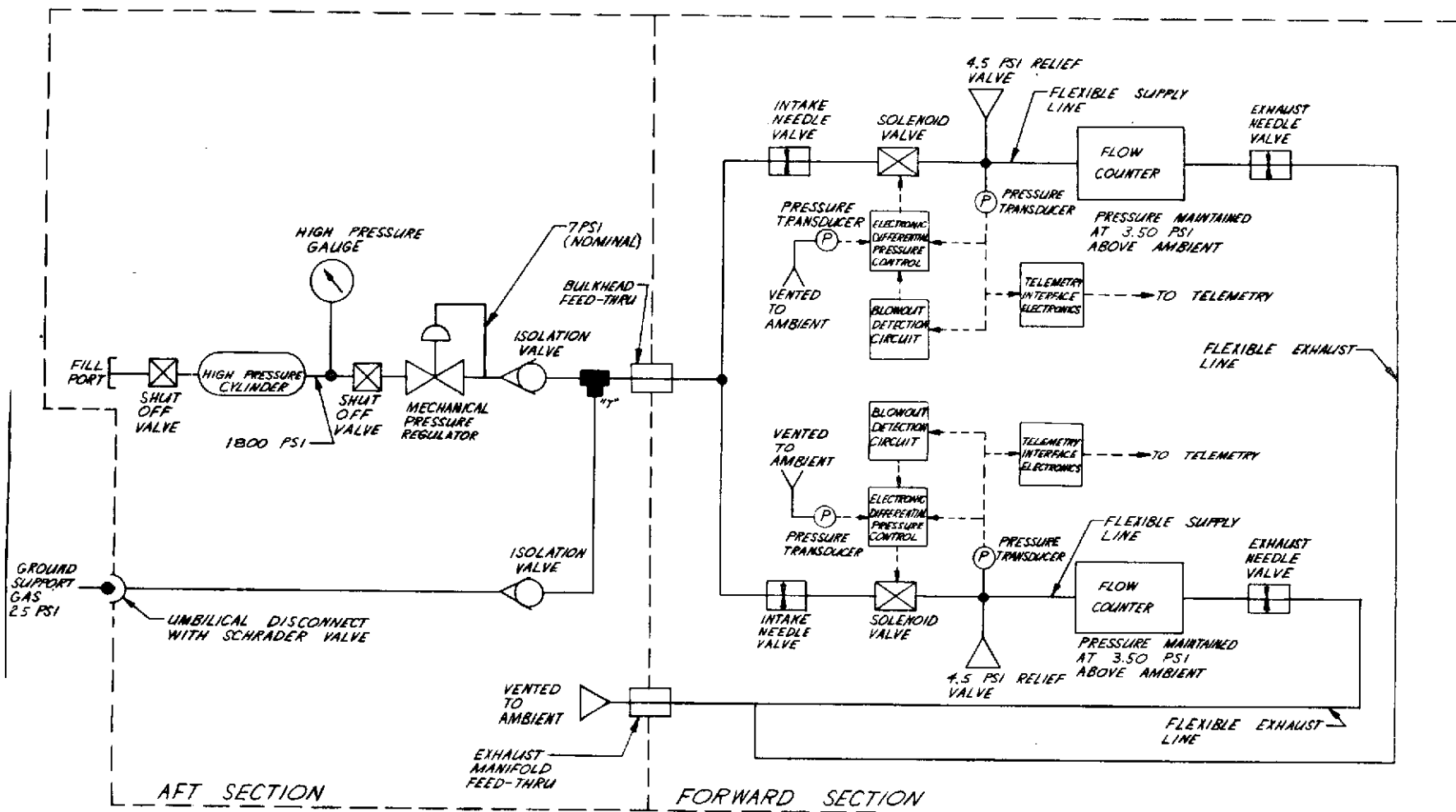


Figure 15. Block Diagram of the Grating Spectrometer Gas Control System

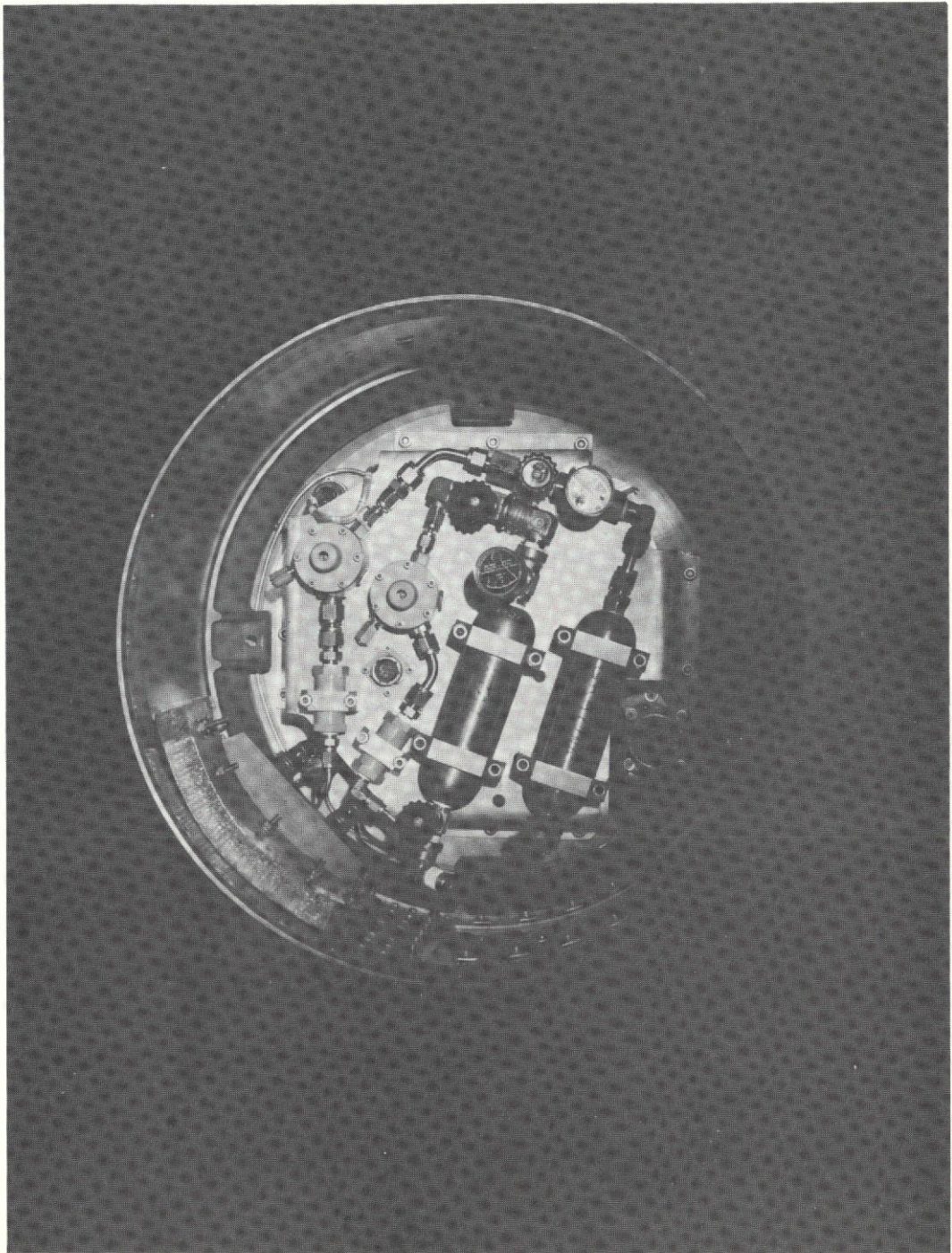


Figure 16. View of Aft Section of Rocket Payload showing Mechanical Components of Gas Handling System for the Flow Proportional Counters

through an intake needle valve and then to a solenoid-operated precision valve. The intake needle valve restricts the flow of gas in the event of a complete blowout of the counter window and also reduces pressure surges or "overshoot" that result from the normal "fill pulses" of the solenoid valve.

The pressure of the flow counter (absolute) is sensed with a solid-state pressure transducer, and the pressure signal is transmitted to the electronic pressure control (EPC), which is described in the next section. The ambient pressure is sensed with an identical transducer and its information is also transmitted to the EPC.

A precision mechanical relief valve is coupled to the flow path in order to purge the system of excess pressure during the rocket's ascent and to protect the fragile detector window from overpressure.

The gas is then fed to the flow counter through a 1/8-in.-diam flexible hose. The exit gas is conducted from the flow counter through an exhaust needle valve and returned to the aft section of the payload through a second flexible hose, where it is vented to the ambient atmosphere. The exhaust needle valve establishes a minimum flow rate during the flight, relieves the excess pressure after the mechanical relief valve closes, and controls the flow of gas on the ground during the prelaunch "counter purge" phase. Venting into the aft section provides a convenient location for exhaust gas handling and flow measurement during the systems tests when the payload is operated in a vacuum chamber.

a. Electronic Pressure Control Theory of Operation

A block diagram of the grating spectrometer EPC and its peripheral electronics is shown in Fig. 17.

The flow counter and ambient pressure signals from the two pressure transducers are connected to a differential amplifier. The pressure difference output signal is fed to a comparator circuit, where it is compared with a preset pressure difference reference.

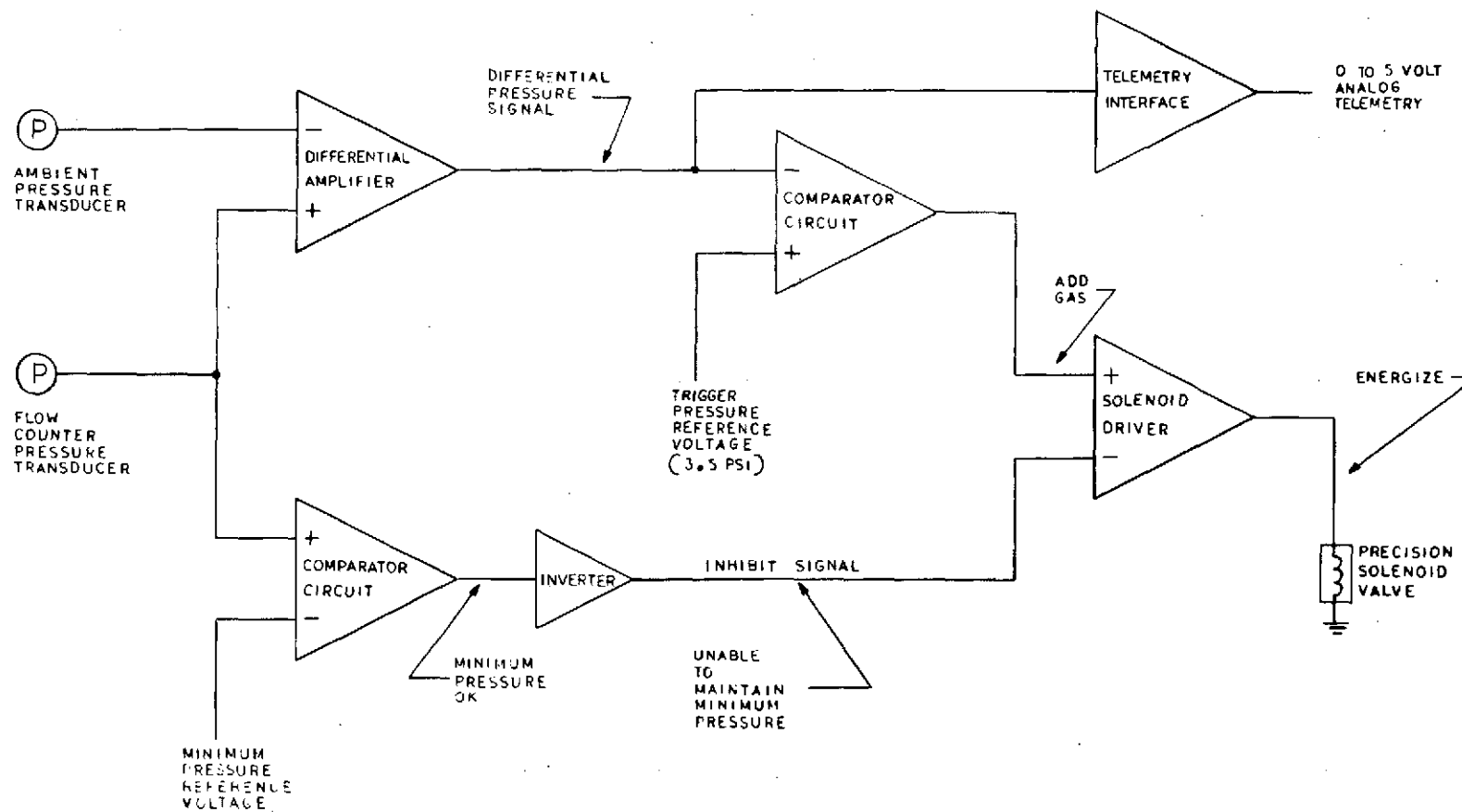


Figure 17. Block Diagram of the Grating Spectrometer Electronic Pressure Control and Peripheral Electronics

It should be pointed out here that the approach taken was to monitor and maintain the differential pressure across the flow counter window rather than switch to a lower absolute pressure at the moment of launch. The latter approach would have possibly allowed the window to relax or unflex at the moment of launch. It was decided that a constant positive pressure would minimize the effects of vibration on the window in the region of its seal and therefore reduce the possibility of tearing. Also, switching to a new reference would not lend itself well to an easy prelaunch checkout. The comparator circuit has sufficient hysteresis to ensure firm, chatterless solenoid operation.

The flow counter pressure transducer is mounted pneumatically close to the gas exit side of the solenoid valve in order to minimize its response time to pressure transients leaving the solenoid. This fast response time to transducer and the hysteresis of the comparator circuit combine, in effect, to form an electronic-pneumatic hybrid one-shot multivibrator that generates single short-duration gas pulses. Each pulse adds approximately 9.3×10^{-6} SCF of gas to the flow counter. The result is a pressure transient of about 1.2 percent, which is visible through the telemetry. The repetition rate of the transients is a function of the gas flow rate and is used as a "window status" check prior to and during the flight. The pressure difference signal is also connected to the telemetry interface circuit, where it is buffered and conditioned to a 0- to 5-V format.

The flow counter pressure transducer is also connected to a comparator circuit that compares the counter pressure (absolute) with a preset value to determine whether or not the GSGCS is supporting the existing leak rate. If the flow counter pressure drops below a minimum value, a "blowout" is indicated, a "gas flow" inhibit signal is transmitted to the solenoid drive circuit, and the system is shut down. The absolute pressure rather than the difference pressure is checked in order to eliminate a "lock out" condition during startup.

b. GSGCS Dynamic Flight Characteristics

The GSGCS is activated 4 hr prior to launch. The flow counter pressure is 3.5 psi above the ambient. This, in the case of a White Sands launch, is about 16.3 psi absolute. Gas is furnished by the ground support supply at a pressure of 25 psi. The flow rate is set by the exhaust needle valve to about 0.05 standard cubic feet per hour (SCFH). The gas pulse repetition rate is about 2 per sec.

At the moment of launch, the umbilical disconnects and the Schrader valve seals. As the rocket ascends, the mechanical relief valve opens and purges the counter of excess pressure, limiting it to about 4.5 psi across the window. This occurs at about $T + 3$ sec. At approximately $T + 35$ sec, the relief valve begins to close, and by $T + 45$ sec, it is closed tight.

The pressure continues to decay due to the venting through the exhaust needle valve. By $T + 50$ sec, the differential counter pressure has dropped back to the 3.5 psi level, and the GSGCS resumes pulsing gas.

The gas trapped in the connecting lines between the umbilical fitting and the intake needle valve constitutes a source of high-pressure gas (25 psi, initially). This high-pressure gas causes substantial overshoot in the gas pulses. The internal volume of these lines was minimized in order to hasten the consumption of this gas, and by $T + 80$ sec, the pressure has dropped to 7 psi. At this point, the GSGCS is supplying gas from the onboard supply.

As the ambient pressure approaches a vacuum, the flow counter pressure approaches an absolute value of 3.5 psi. The flow rate settles to about 0.015 SCFH, with a gas pulse repetition rate of about 2.5 per sec. At this rate, the onboard gas supply can last approximately 14 hr.

The maximum flow rate tolerable is about 0.76 SCFH per flow counter. At this rate, the onboard gas supply can last approximately 17 min.

2. CRYSTAL SEPECTOMETER GAS CONTROL SYSTEM

The function of the crystal spectrometer gas control system (CSGCS) is to supply a gas mixture of 25 percent xenon, 10 percent methane, and 65 percent argon to the flow proportional counters of the crystal spectrometer during the prelaunch and active measurement phases of the rocket's flight. During the prelaunch phase, the CSGCS is active several hours prior to launch to permit a systems checkout and to purge the flow counters of contaminants and moisture. External gas is supplied to the CSGCS through an umbilical in order to conserve the onboard gas supply.

The crystal spectrometer operates in a shorter wavelength region than the grating spectrometer, and the flow counter window transmission requirements are less severe. For this reason, thicker and less fragile windows can be used. Also, counter gain can be lower because of the higher-energy photons. This permits an operating pressure of 1 atm while maintaining reasonable voltages on the detectors. A slightly higher pressure was selected (16 psi) to ensure stable gas flow during prelaunch activities. A block diagram of the CSGCS is shown in Fig. 18.

For the sake of brevity, the following description only points out the differences between the CSGCS and the GSGCS as the two systems are similar in design. The CSGCS contains hardware identical to the GSGCS, including the onboard high-pressure gas supply cylinder, umbilical fitting, isolation valves, needle valves, supply and exhaust flexible lines, solenoid valves, and flow proportional counters. No mechanical relief valve is required, as in the GSGCS, because the CSGCS maintains a constant not a differential absolute pressure in its flow counters. The venting of excess gas is not necessary, and the need to monitor the ambient pressure has also been eliminated.

The onboard gas supply is about 0.41 SCF at 1800 psi. The onboard mechanical pressure regulator is set for 22 psi, and the flow counter pressure are set for 16 psi. The exhaust needle valves are adjusted to establish the minimum prelaunch flow rate (0.01 SCFH) necessary to purge contaminants.

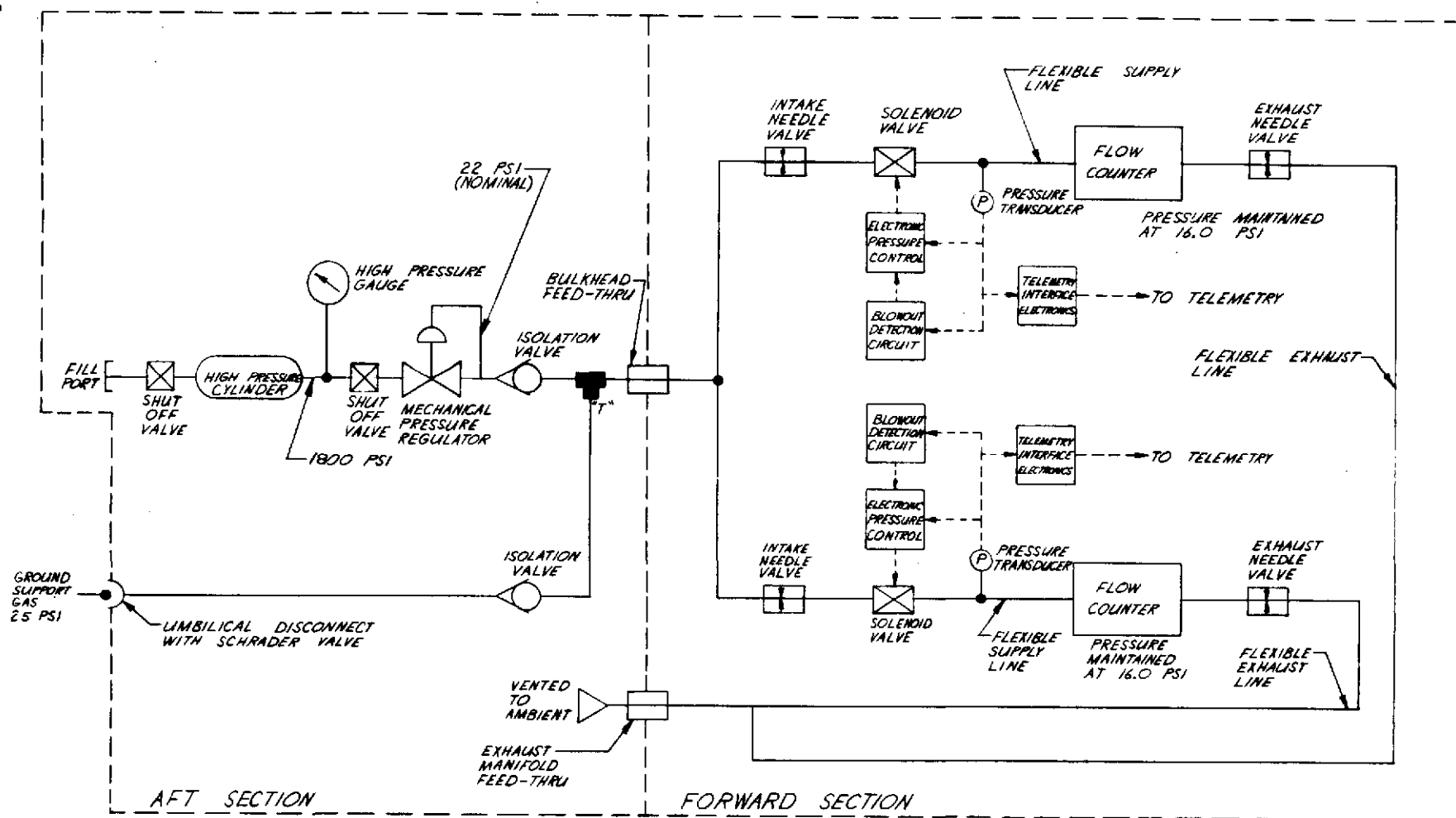


Figure 18. Block Diagram of the Crystal Spectrometer Gas Control System

A block diagram of the crystal spectrometer EPC is shown in Fig. 19. Note that no differential amplifier (difference) was necessary, and that the flow counter pressure signals are fed directly to the gas pressure control and window blowout comparator circuits.

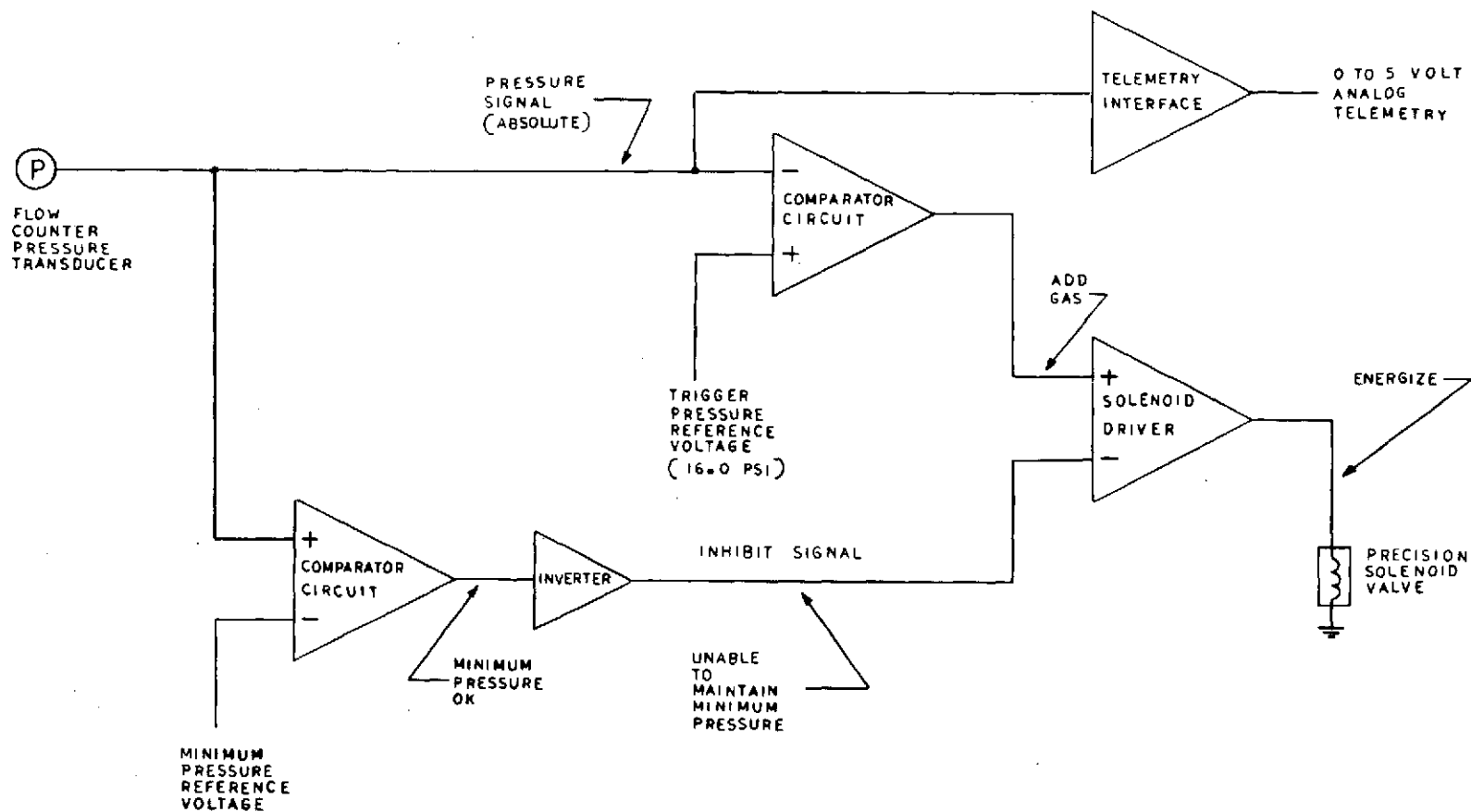


Figure 19. Block Diagram of the Crystal Spectrometer Electronic Pressure Control.

VII. GRAZING INCIDENCE X-RAY TELESCOPE

The grazing incidence x-ray telescope included in the rocket payload is essentially a one-third scale version of the S-056 x-ray telescope flown on the ATM/Skylab missions. The rocket telescope was previously flown on an Aerobee rocket on October 1967 in a test of the S-056 optical concept.

The telescope itself is of the Wolter type 1 configuration, which consists of a primary paraboloidal element followed by a confocal hyperboloid. This system operates at a glancing angle of 54 arc min and has a focal length of 63.4 cm and a projected frontal area (collecting area) of 1.6 cm^2 .

The two optical elements were ground and polished from fused silica and figured to the correct parabolic and hyperbolic shapes by Perkin-Elmer Corporation. The telescope is one of two made in late 1966 for NASA-Goddard Space Flight Center.

An eight-sided turret, driven by a clockwork mechanism, rotates eight separate discs of x-ray sensitive film into the image plane. Each piece of film was mounted in a separate miniature cassette that incorporates an x-ray filter. Five separate filters were used: four were identical to those used in the S-056 experiment (1/4 and 1/2 mil aluminum, 3 mil beryllium, and 1/10 mil titanium); the fifth was aluminum-coated mylar, 0.15 mil thick with a $1000\text{-}\text{\AA}$ coat of aluminum on each side. The film discs were punched out of a film roll with a specially designed punch. Type 101-01 film (a Schumann emulsion) was used for this flight. Type SO-212 film used in the ATM S-056 and S-054 experiments was not used because it was not possible to use a safe-light with this film to determine which side of the punched disc the emulsion was on.

For the rocket flight, the telescope was removed from its original housing and the two elements separated and cleaned. The two elements were then realigned to each other by shrinking an aluminum band on the outside of the elements and then mounted in a new and more compact cell. In this new

cell, the elements were restrained by circumferential and end 'O'-rings to provide a soft mount and to prevent fracture of the silica during launch.

Focusing of such a small telescope is a problem because of the large depth of field in visible light and the difficulty of obtaining a perfectly parallel beam of x rays for testing. This problem has been solved by other groups by using a long pipe with an x-ray tube at one end to produce a quasi-parallel beam, and then calculating the focus shift required to correct for the case of an infinitely distant object. Another scheme uses a normal incidence paraboloidal mirror to collimate He II 304 Å radiation; the telescope is then focused in the EUV, where the diffraction effects are much less severe than they are in visible light. Because of time and cost limitations, it was not possible to adopt either of these approaches with the rocket x-ray telescope. Therefore, efforts were made to focus the telescope by using white light from a collimator. It was difficult to judge the best focus by eye, and a photodiode with a pinhole aperture in front of it was inserted into the focal plane. This method gave only marginally improved discrimination of the position of best focus. The telescope was eventually focused by a combination of these two methods, but it is likely that the optimum position for best x-ray focus was not found.

VIII. MONITOR PROPORTIONAL COUNTER SYSTEM

A. DESCRIPTION

A block diagram of the monitor proportional counter system is shown in Fig. 20. A small proportional counter was required to view the sun through the grating spectrometer entrance collimator to act as an x-ray flux monitor. An LND model 421 was chosen because of its small size and ready availability. This is a rectangular counter with a 3/4-in.-square cross section and 1/2-in.-diam circular window. In order to maximize efficiency, a 1 atm 90% Xe + 10% CH₄ fill and a 1-mil beryllium window were used.

The counters were tested for linearity and resolution by using monochromatic x-rays of several different energies. X-rays produced by a Henke-type source passed through a thin window to strike targets made of various materials. These targets produced the characteristic fluorescent x rays for the measurement. The beam was monochromatized by Bragg reflection from a crystal and onto the detector window. With this technique, the following monochromatic x rays were produced: Cu L α (0.93 keV), Zn L α (1.01 keV), Mg K α (1.25 keV), Al K α (1.49 keV), Si K α (1.74 keV), Mo L α (2.29 keV), Cl K α (2.26 keV), In L α (3.29 keV), and Sn L α (3.44 keV). In addition, Mn K α x rays (5.89 keV) were produced by an Fe⁵⁵ radioactive source. All the tests were performed in vacuum.

Two proportional counters were used for all of the tests. The two were nearly identical in performance; both had excellent linearity. The full-width at half-maximum resolution for photons of energy $h\nu$ fit power law curves well. The expression were: $\text{FWHM} = 0.37(h\nu)^{0.56}$, for counter A; $\text{FWHM} = 0.375(h\nu)^{0.59}$, for counter B. The theoretical shape of this type of function is $\text{FWHM} = A(h\nu)^{0.50}$. The FWHM for an Fe⁵⁵ source was 17 percent for counter A and 18 percent for counter B. Counter A was used in the rocket flight; counter B was used as a backup.

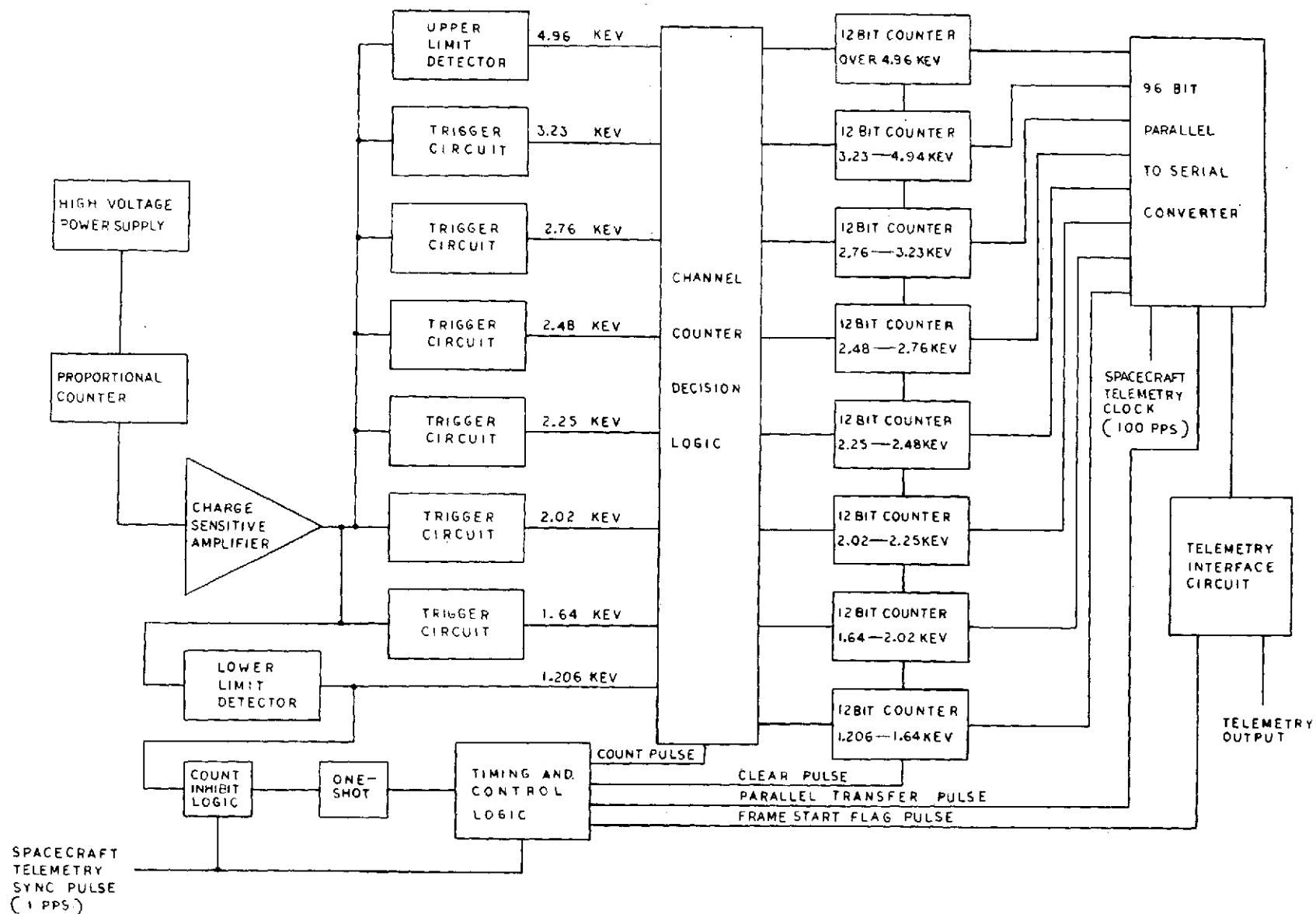


Figure 20. Block Diagram of the Monitor Proportional Counter System

The output of the proportional counter is fed to a charge-sensitive amplifier, which drives an eight-channel pulse height analyzer that consists of eight parallel input trigger circuits. Each trigger circuit is composed of a comparator circuit with a threshold preset to a given energy. The lowest energy trigger circuit serves as a lower-level detector or discriminator. It also starts the necessary timing sequences of each event.

The trigger circuit outputs are connected to the channel counter decision logic (CCDL), which selects the appropriate channel counter to be activated by noting the highest energy trigger circuit in the "on" state. The requirement of only eight pulse height channels justified the direct threshold approach by eliminating the need for sample-and-hold and analogue-to-digital circuits. It also simplified the channel counter logic.

Eight 12-bit ripple counters are fed by the CCDL, giving each channel a maximum count rate of 4096 cps when sampled once per second by the telemetry. The count inhibit logic halts the pulse height analysis process each time a telemetry sync pulse is received. This allows the ripple counter propagation delay time to settle before the count data is transferred to the parallel to serial converter.

The lower level detector (lowest energy trigger circuit) feeds a "one-shot" that generates a single pulse each time a minimum energy (1.20 keV) event occurs. This pulse drives the timing and control logic (TCL).

The TCL generates a pulse that is steered to the appropriate channel counter by the channel counter decision logic. The TCL also controls the 96-bit parallel transfer of data from the channel counters to the parallel to serial converter, resets the counters after each data transfer, and restarts the pulse height analysis process.

The parallel-to-serial converter operates independently from the counters and generates a serial frame that consists of eight words of 12 bits each followed by a four-bit "frame sync" word, which actually contains an elevated pedestal bit for sync recognition. This is permissible because the

telemetry is analog (0 to 5 V). The generated binary levels are 0 to 3.5 V for data and 4.5 V for sync. The data rate is 100 bps.

B. MONITOR SYSTEM CALIBRATION

The relative thresholds (ratios of energies) of all eight pulse height channel trigger circuits were adjusted to their appropriate values. Then, a precision attenuator (value = 0.469) was inserted between the charge sensitive amplifier and the trigger circuit input. An Fe^{55} radioactive source ($E = 5.89 \text{ keV}$) was placed in front of the proportional counter, and the high voltage supply was adjusted to maximize the counting rates in the appropriate channels. This voltage setting was used during the rocket flight.

The following is a list of the monitor system channel energies:

- No. 1, 1.20-1.64 keV
- No. 2, 1.64-2.02 keV
- No. 3, 2.02-2.25 keV
- No. 4, 2.25-2.48 keV
- No. 5, 2.48-2.76 keV
- No. 6, 2.76-3.23 keV
- No. 7, 3.23-4.94 keV
- No. 8, 4.94 keV and up